Karlsruhe Institute of Technology

Institute of Fluid Mechanics

# Numerical Simulation of Droplet Impact and Rebound on a Wall

Numerische Simulation von Tropfenaufprall und -abprall an einer Wand

Master Thesis of

Yanchen Wu

At the Department of Mechanical Engineering,
Institute of Fluid Mechanics

Advisors: Dr.-Ing. Xuan Cai
Dr.-Ing. Martin Wörner
Prof. Dr.-Ing. Bettina Frohnapfel

Duration: May 2017 – September 2017

I declare that I have developed and written the enclosed thesis completely by myself, and have not used sources or means without declaration in the text.

**Karlsruhe, 15. 09. 2017**

.....

(**Yanchen Wu**)

# Abstract

The study is devoted to the numerical simulation of droplet impact and rebound on a horizontal surface. The phase-field method (PFM) is used. It is firstly validated for several cases from literature concerning the spreading characteristics of the impact of a single droplet and the coalescence of two droplets. All the numerical results are in good match with experimental data from literature. The numerical method is then applied to study the impact behavior of a single AdBlue droplet under different conditions. Several drop-impact regime maps for physical parameters such as contact angle $\theta$ (90-170$^{o}$), impact velocity $U$ (0.01-10 m/s) and droplet diameter $D$ (0.01-3 mm) are generated, in which the deposit and rebounce regime are identified. Then, a regime map based on dimensionless parameters Weber number $We$ (0.05-4) and Reynolds number $Re$ (100-800) is generated, showing good agreement with experimental data from literature. Furthermore, regime maps based on Weber number $We$ and contact angle $\theta$ for droplets of different sizes are generated. The regime map for smaller droplet shows no good agreement with the model from literature. At last, the effect of coalescence of two simultaneously impacting droplets on the rebound is investigated with this numerical method.

# Contents


**1. Introduction** **1**

**2. Fundamentals** **3**
2.1. Physical Fundamentals . . . 3
2.1.1. Wetting Phenomenon . . . 3
2.1.1.1. Wettability and Contact Angle . . . 4
2.1.1.2. Contact Angle Hysteresis . . . 4
2.1.2. Droplet Impact . . . 5
2.1.2.1. Important Parameters . . . 5
2.1.2.2. Classification of Outcomes of the Droplet Impact . . . 5
2.1.2.3. Spread Factor and Stages of Spreading . . . 6
2.1.3. Coalescence of Droplets . . . 7
2.2. Mathematical Formulation . . . 8
2.2.1. Cahn-Hilliard-Navier-Stokes Equations . . . 8
2.2.2. Discussion of Phase-field Parameters . . . 10
2.2.3. Numerical Methodology . . . 11

**3. Study of Single Droplet Impact and Rebound** **12**
3.1. Validation 1: Spread Factor and Morphology Evolution . . . 12
3.1.1. Physical Properties and Computational Setup . . . 12
3.1.2. Numerical Parameter Study . . . 13
3.1.3. Comparison with Experimental Results for Morphology Evolution . . . 15
3.2. Validation 2: Maximal Spread Factor . . . 16
3.3. Validation 3: Contact Time with the Wall . . . 17
3.4. Study of the Impact Behavior of a Single AdBlue Droplet . . . 20
3.4.1. Effects of Physical Parameters . . . 20
3.4.2. Regime Maps for Physical Parameters . . . 23
3.4.3. Regime Maps based on Dimensionless Parameters . . . 25

**4. Study of Coalescence of Two Droplets** **28**
4.1. Validation 1: Coalescence of a Falling Droplet and a Sessile Droplet . . . 28
4.2. Validation 2: Coalescence with Rebound . . . 31
4.3. Effect of Coalescence on Rebound . . . 33

**5. Summary and Outlook** **36**

**Symbols and Abbreviations** **38**

**List of Figures** **40**

**List of Figures** **42**

**Bibliography** **43**

**Appendix** **46**
A. OpenFOAM Codes . . . . . 46
A.1. Function for capturing the base diameter of a droplet . . . . . 46
A.2. Function for capturing the height of droplet centroid . . . . . 47
B. The Regime Limit Model of Caviezel . . . . . 47

# 1. Introduction

The selective catalytic reduction (SCR) based on urea-water-solution (AdBlue) is an effective and reliable method to reduce nitrogen oxides ($NO_x$) in the exhaust gas of engines [3, 4, 12, 19, 20]. The Urea-water-solution needs to be sprayed into the exhaust gas flow upstream of the SCR catalyst. The droplets evaporate and the urea is decomposed into ammonia, which converts $NO_x$ into nitrogen and water [19, 20]. The spray/wall-interaction (see Figure 1.1) has a great influence on the efficiency and lifespan of the system. If the sprays come onto the wall, there could exist a liquid film, which can lead to deposition of solids. After a certain time, the accumulation of deposit can damage the system. It is therefore of importance to investigate, to what extent the liquid film and deposit formation can be minimized or prevented. To gain enough knowledge and solve this technical problem, the spray/wall-interaction needs to be studied in more detail.

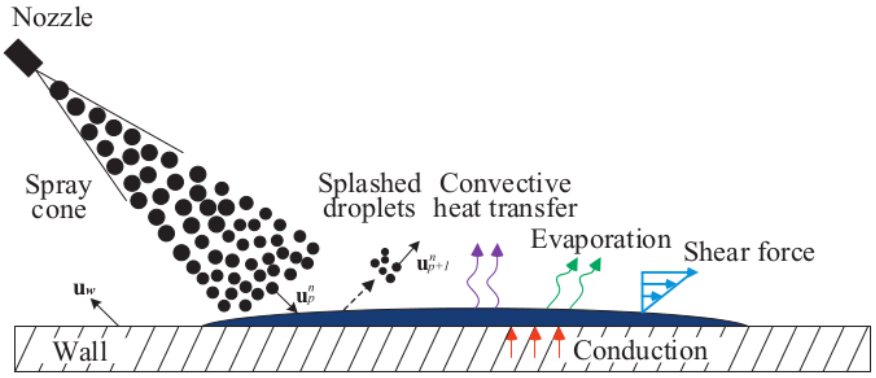


Figure 1.1.: Spray/Wall-Interaction. Taken from [47].

This work focuses mainly on the numerical simulation of the impact of a single droplet onto a solid wall. Particularly, it needs to be studied in detail, under which condition the droplet can rebound since the rebound can extend the residence time of droplets in the exhaust stream. This improves the ammonia conversion rate of AdBlue drops and can reduce or prevent the formation of liquid film and deposit. Through parameter studies, it is to be investigated, how the wall properties and the operating parameters influence the impact and rebound behavior of a single droplet. Besides, coalescence of drops is also numerically studied. Considering the operating conditions of the SCR system, there could exist coalescence of droplets on the wall, which makes it easier to form a liquid

film and therefore needs to be investigated. Several cases of coalescence of two droplets are simulated in chapter 4. The simulations concerning rebound behavior and coalescence can contribute to the determination of optimal operating parameters and thus help us to design a reliable SCR system.

In this work, the phase-field method is coupled with the single-field Navier-Stokes equation to simulate the impact process and coalescence of droplets. The phase-field method is especially suitable for the simulation of droplet spreading on solid surfaces, because it solves the paradox between the moving contact line and the no-slip boundary condition on the solid surface [15, 21]. Besides, the phase-field method is also appropriate to simulate coalescence of droplets, since the perspective of modeling fluid interfaces as having small but finite thickness makes it easier to handle the problem of topological transition of interfaces [24]. The remainder of this thesis is structured as follows.

Chapter 2 introduces the physical and mathematical fundamentals. The important phenomena with basic concepts are explained in detail. Furthermore, the phase-field model and the coupling of Navier-Stokes equation with Cahn-Hilliard equation are presented.

In chapter 3, the numerical method is validated for single droplet rebound against experimental data from literature. Three validations in terms of spread factor and morphology evolution, the maximal spread factor and contact time are carried out. After the validations, the impact behavior of a single AdBlue droplet under different conditions is investigated. The effects of contact angle ($\theta$), droplet diameter ($D$), and impact velocity ($U$) are studied. Based on these, three drop-impact regime maps are generated, in which deposit and rebounce regime are identified. Regime maps for dimensionless parameters are also generated to compare with experimental data and theoretical model from literature.

In chapter 4, a few cases of coalescence of two droplets are simulated and compared with experimental data from literature. In these cases, coalescence with impact process or with rebound is involved. After that, the effect of coalescence on the droplet rebound is discussed.

Chapter 5 provides summaries of the whole work and the outlooks.

The numerical simulation facilitates the analysis of the influence of the key factors on the droplet spreading process and coalescence phenomena and helps us to understand the underlying physical mechanism. Furthermore, it can reduce the effort required in the development of SCR system.

# 2. Fundamentals

The dynamic of the impact and coalescence of droplets on a solid wall are through numerical simulation investigated. The related physical phenomena in terms of wetting, droplet impact and coalescence are introduced. Then, mathematical formulation of these hydrodynamical processes, which is based on the coupling of the phase-field model with Navier-Stokes equation, is presented.

## 2.1. Physical Fundamentals

Basic concepts of the physical phenomena are demonstrated in this section.

### 2.1.1. Wetting Phenomenon

The phenomenon of a liquid to maintain contact with a solid surface is called wetting. Wetting is therefore in nature a liquid interaction at solid-gaseous interfaces. It describes how a liquid comes into contact with a solid surface [18]. All the surfaces we mentioned below are ideally smooth, chemically homogeneous, rigid and inert. The wetting phenomena are very common both in nature and in industry. One of the most famous example in nature is the lotus effect (see Figure 2.1). Due to the microscopic textures of the leaf surface, a droplet of water rolls off the surface easily or stays there and keeps a form of spherical shape. This surface shows excellent hydrophobicity, i.e. great water repellency. In industrial branches, the wetting processes appear in applications such as inkjet printing, digital

Figure 2.1.: Lotus effect. Taken from [5].

printing, spray painting and coating and so on. A comprehensive understanding of wetting phenomenon can potentially lead to technological improvement in these engineering fields.

#### 2.1.1.1. Wettability and Contact Angle

The notion of wettability was first mentioned by Young in 1805 [43]. In order to quantitatively describe wetting phenomenon, the concept of contact angle was proposed. The static contact angle or Young's angle $\theta$ indicates the tangential angle at liquid-solid-air interface (see Figure 2.2). Based on mechanical equilibrium of the three interfacial tensions, the Young's equation is expressed as follows:

$$\gamma_{SV} = \gamma_{LV} \cdot \cos\theta + \gamma_{SL} \tag{2.1}$$

Therein $\gamma_{SV}, \gamma_{LV}$ and $\gamma_{SL}$ are gas-solid interfacial tension, liquid-gas interfacial tension (surface tension) and liquid-solid interfacial tension, respectively. From the Young's equation, it can be concluded that the contact angle is determined by the three interfacial tensions.

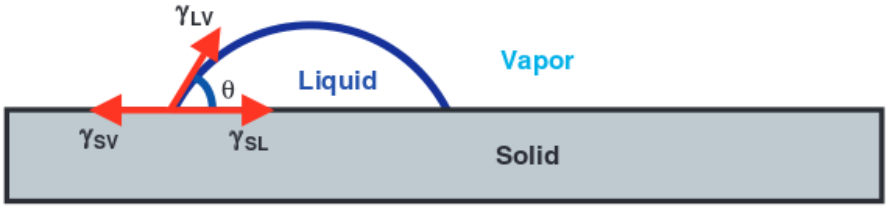


Figure 2.2.: A drop on a flat surface. Taken from [23].

The contact angle describes the wettability of a surface. A low contact angle indicates surfaces on which a droplet tends to spread and shows big contact area between the droplet and the surface. In this situation, the surface is endowed with a characteristic of hydrophilicity. On the contrary, a high contact angle symbolizes unwettable surfaces, on which the contact area is very small. The surface shows a property of hydrophobicity.

Quantitatively speaking, surfaces whose contact angle is less than 90°, are defined als hydrophilic surfaces. Surfaces with contact angle higher than 90° are hydrophobic ones. Superhydrophobic surfaces are those whose contact angle is typically higher than 150°. Figure 2.3 shows different wettability of the surface from contact angle 0° to 180°.

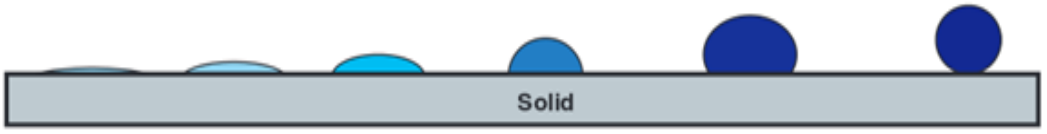


Figure 2.3.: Contact angle and wettability. Taken from [23].

#### 2.1.1.2. Contact Angle Hysteresis

From Young's equation, it seems that there is only one value of contact angle. However, in reality, the equilibrium contact angle ranges from advancing contact angle $\theta_A$ to receding contact angle $\theta_R$, which are the maximal and minimal values of the contact angle [38]. Contact angle hysteresis is defined as the difference between advancing contact angle $\theta_A$ and receding contact angle $\theta_R$. The reason for the existence of contact angle hysteresis

is the roughness and heterogeneity of surfaces. According to Law et al. [22], the contact angle hysteresis indicates the difference in liquid-solid interfacial tension during advancing and during receding. In this work, the surface is assumed to be ideally smooth and the contact angle hysteresis phenomenon is not taken into account.

### 2.1.2. Droplet Impact

The dynamics of liquid droplets impacting on a solid surface has been studied for over 140 years. It was firstly studied by Worthington in the year 1876 [41]. However only within the past 20 years, when high-speed video technology allows time-resolved observations of this phenomenon, the rapid dynamics of the impact process can be explained. On the other hand, with increasing computational power and improved numerical algorithms, more details of this phenomenon can be simulated [16]. Further understanding of the underlying mechanism can be therefore achieved.

#### 2.1.2.1. Important Parameters

The different parameters involved in the droplet impact process are to be defined. In the present study, a single spherical droplet impacting normal on an ideally smooth solid surface is investigated. The impact process is affected by various factors including droplet properties (droplet diameter $D$, dynamical viscosity $\mu_l$, density $\rho_l$, surface tension $\sigma_l$, etc.), properties of the surrounding gas (dynamical viscosity $\mu_g$, density $\rho_g$ etc.), kinematic parameters (droplet impact velocity $U$, gravitational acceleration $g$), surface property of the solid wall (contact angle $\theta$).

To represent effects of these physical parameters above, six dimensionless parameters are defined. Reynolds number, $Re = \rho_l DU/\mu_l$, Weber number, $We = \rho_l DU^2/\sigma_l$, Froude number, $Fr = U/\sqrt{gD}$, Capillary number, $Ca = \mu_l U/\sigma_l$, Ohnesorge number, $Oh = \mu_l/\sqrt{\rho_l D\sigma_l} = \sqrt{We}/Re$, Stokes number, $St = \mu_g/(\rho_l DU) = \mu_g/(\mu_l Re)$.

$Re$ is the ratio between inertia and viscous forces, while $We$ is the ratio between the inertia and the capillary forces. $Fr$ indicates the quotient between inertia and gravity. Liquid droplets are usually in the millimeter range and in this work, the Adblue drops near the solid wall are even much smaller. In this condition, $Fr \gg 1$, and gravity can be neglected. $Ca$ stands for the relative importance of viscous to capillary force. $Oh$ indicates the influence of the viscosity and relates the viscous force to inertial and capillary forces. $St$ quantifies the influence of the gas in the lubrication layer beneath the drop before impact [16], which is regardless in this study.

In general, the impact dynamics are characterized by $Re$ and $We$. Alternatively, $Oh$ and $Ca$ are also used in the literature. Considering the impacting conditions in the present study, $Re$ and $We$ are chosen to describe the impact dynamics.

#### 2.1.2.2. Classification of Outcomes of the Droplet Impact

During the droplet impact process on a solid surface, six phenomena can appear under different conditions, i.e., deposition, prompt splash, corona splash, receding break-up, partial rebound and complete rebound [34]. Figure 2.4 shows the morphology of the droplet of the six phenomena.

For deposition, the droplet spreads over the surface and then stays at rest. The prompt splash exists when the droplet impacts on a rough surface with relative high velocity. If the surface tension is reduced, the liquid lamella can detach from the wall, forming a corona splash. As the droplet is impacting on the wall until the end of the spreading stage, the kinetic energy is partly dissipated by viscous forces and partly converts into the surface energy [42]. The subsequent behavior of the lamella depends on to what extent the kinetic energy is dissipated. Owing to the contact angle hysteresis, nonwettable surface and capillary instability, the receding breakup scenario can appear. If the surface energy and kinetic energy of the lamella at the end of the spreading stage still large enough, then

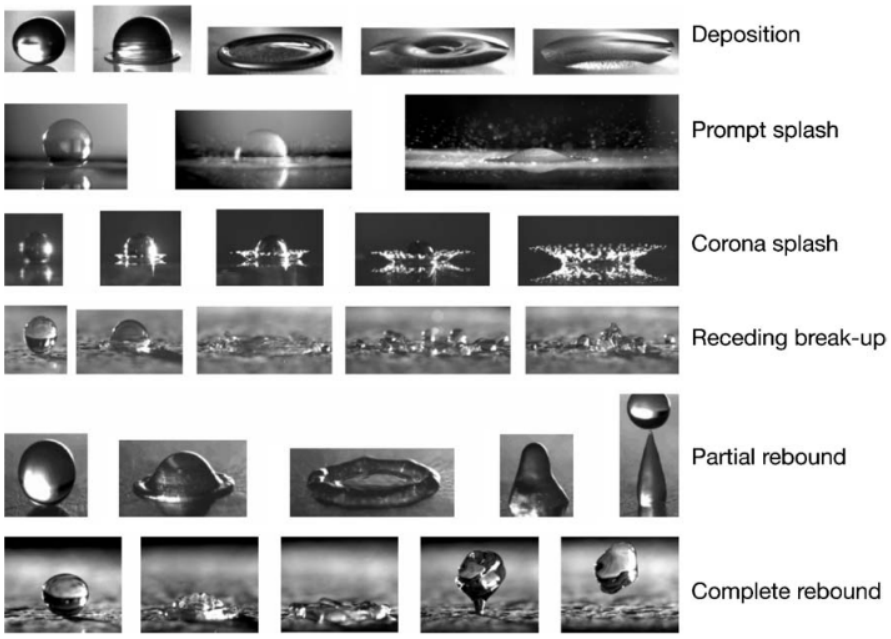


Figure 2.4.: Morphology of droplet impact on a dry surface. Taken from [34].

complete rebound happens. If the surface energy and kinetic energy is fully dissipated during the receding stage, then partial rebound comes into being. In this work, we only focus on the scenarios of deposition and complete rebound. In chapter 3, we will discuss under what conditions the droplet can completely rebound.

#### 2.1.2.3. Spread Factor and Stages of Spreading

The spread factor $\beta$ is defined as the ratio between the instantaneous base diameter of the droplet on the wall $D_t$ and the initial droplet diameter $D_0$:

$$\beta = \frac{D_t}{D_0} \tag{2.2}$$

For the droplet impact process, situations are considered, in which no splashing occurs. In these situations, the droplet deforms, then a lamella is formed, which spreads radially on the solid surface until a certain value of the base diameter is reached. Then, the liquid recedes or continues to spread, depending on the different wettability and the impact conditions. After an oscillation process, the drop settles down with a certain form on the solid surface.

The time evolution of the spread factor can be therefore divided into four phases: the kinematic phase, the spreading phase, the relaxation phase and the wetting/equilibrium phase [33]. The time evolution of the spread factor and the four phases are presented in Figure 2.5. The time $t^* = tU/D_0$ is non-dimensionlized by using impact velocity $U$ and initial diameter of the droplet $D_0$. The lines of different types correspond to different situations of spreading, which depends on the impact conditions. For the first stage, i.e. the kinematic phase, the drop shows a form of a truncated sphere and no spreading lamella appears. There is almost no difference among these different spreading curves. The contact line movement in this stage depends only on geometric conditions. In the second stage, the spreading phase, there exits a thin film bounded by a rim. Different material and dynamic parameters would affect the spreading process. The third stage is the relaxation phase. In this stage, the droplet recedes, rests or still oscillates until a stable state is reached. The last stage is wetting/equilibrium phase. Figure 2.6 (a)-(f) show representative instant

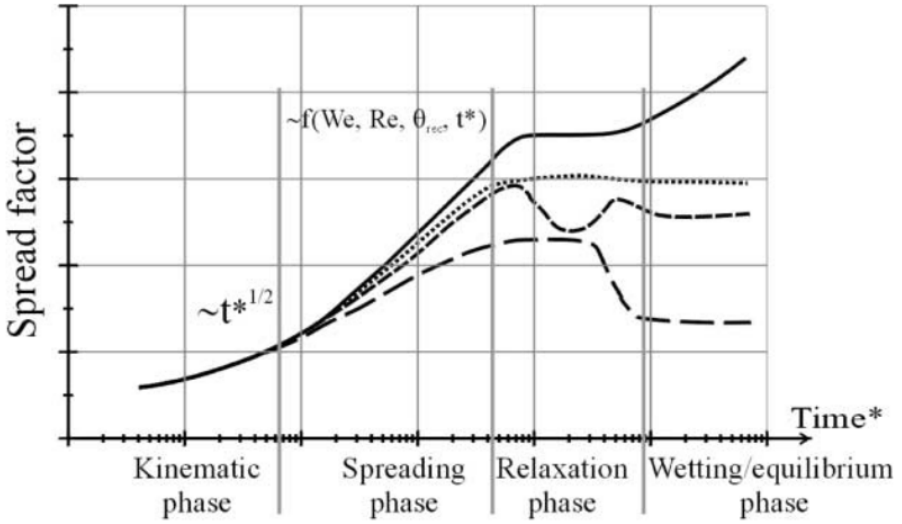


Figure 2.5.: Time evolution of spread factor. Taken from [33].

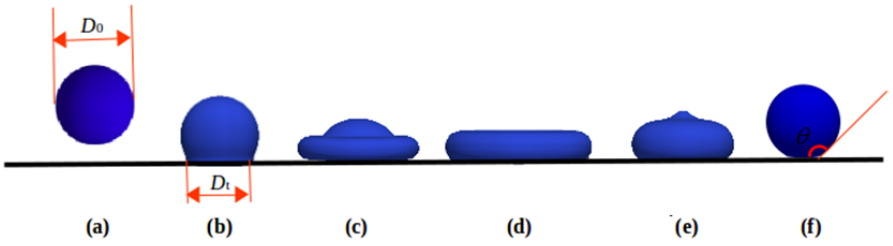


Figure 2.6.: Instant states of droplet of the present simulation. (a) The initial state. (b) The kinematic phase. (c) The spreading phase. (d) The maximum spreading. (e) The relaxation phase. (f) The wetting/equilibrium phase.

states of a droplet for different phases.

### 2.1.3. Coalescence of Droplets

If more than one droplet is considered, there may exist coalescence. The understanding of the dynamics of coalescence is essential for achieving precise control of the droplets behaviors.

The process of the coalescence of two sessile drops can be divided into three stages. Figure 2.7 shows the whole process of the coalescence. Firstly, the two drops connect with each other, then the neck grows rapidly at the connection point, which is driven by surface tension [9]. After this stage, the neck widens and it changes from concave to convex, and an elliptic contact line is created. At last, a spherical cap is formed after several oscillations.

Coalescence is a fluid dynamical event, whose biggest challenge lies in the modeling the features of a free surface and a dynamic contact line [37]. Numerical simulation of coalescence is performed in chapter 4.

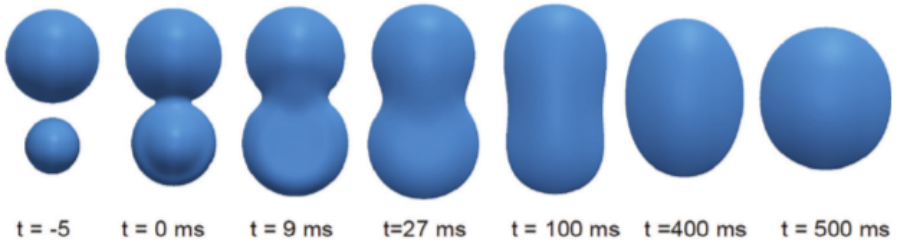


Figure 2.7.: Bird-View onto the coalescence of two drops on a horizontal surface. Taken from [10].

## 2.2. Mathematical Formulation

In order to accurately simulate the dynamic spreading process of a droplet, it is vital to capture the motion of the contact line of the three phases. In contrary to conventional sharp interface methods (e.g. VOF method), which suffer from the paradox between the moving contact line and the no-slip boundary on the wall, the phase-field method is free from this problem via a diffusive mechanism [15]. Based on this, the phase-field method is a promising method for handling moving contact lines. Moreover, the phase-field method with diffuse interface characteristics treats the interface as finite thickness, which makes it easier to handle topological transition of interface (e.g. coalescence of droplets). In this part, the phase-field method and its governing equations are introduced. Then the implementation of phase-field method is briefly presented.

### 2.2.1. Cahn-Hilliard-Navier-Stokes Equations

The phase-field method models fluid interfaces as having finite thickness. The movement and deformation of the interface can be computed on fixed grids [14]. This diffuse interface method models interfacial forces with a chemical potential and therefore the diffuse interface model for multiphase Navier-Stokes flow is easier to solve, which is the biggest advantage compared with the sharp interface method. Figure 2.8 shows the difference of the diffuse and sharp interface model.

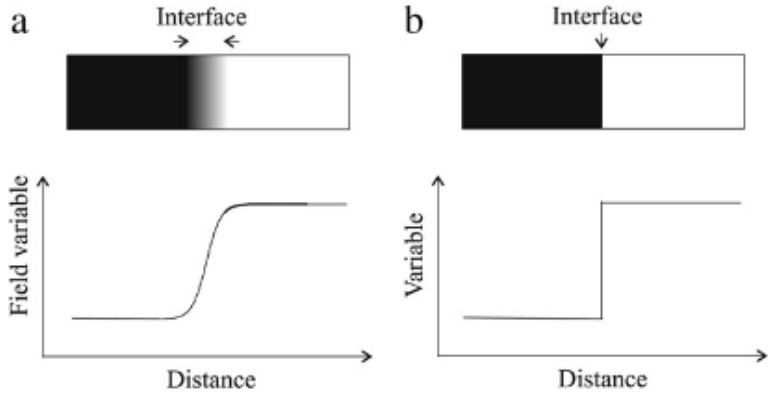


Figure 2.8.: Diffuse and sharp interface model. Taken from [29].

The phase-field method is based on the concept of fluid free energy. The model of free energy density is [45]:

$$f = \frac{1}{2}\lambda \left|\vec{\nabla} C\right|^2 + \frac{\lambda}{4\varepsilon^2}(C^2-1)^2 \tag{2.3}$$

where the first term is gradient energy or interfacial energy and the second term is the bulk energy. $\lambda$ is free energy density parameter. $\varepsilon$ is capillary width, which indicates the thickness of diffuse interface. $C$ is order parameter and characterizes the two different phases. $C$ varies rapidly but smoothly in the thin transition layer and takes the value of 1 and -1 for the bulk liquid and gas phases, respectively (see Figure 2.9).

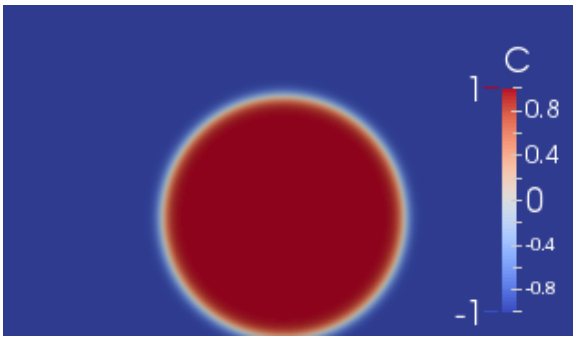


Figure 2.9.: Distribution of $C$ for a droplet.

The free energy of this binary fluid system is then:

$$F = \int_V f \mathbf{d}V \tag{2.4}$$

where $V$ is the system domain.

The chemical potential $\phi$ is defined as the variational derivative of free energy $F$ with respect to the order parameter $C$:

$$\phi = \frac{\delta F}{\delta C} = \frac{\lambda}{\varepsilon^2} C(C^2 - 1) - \lambda \nabla^2 C \tag{2.5}$$

For an equilibrium system, the capillary width $\varepsilon$, the mixing energy density $\lambda$ and the interfacial tension $\sigma$ fulfill the equation:

$$\lambda = \frac{3\sqrt{2}\sigma\varepsilon}{4} \tag{2.6}$$

therefore, the chemical potential $\phi$ depends on capillary width $\varepsilon$, order parameter $C$ and interfacial tension $\sigma$. If the free energy $F$ of the system is minimized, the equilibrium interface profile will be obtained, which is a one-dimensional ($x$-direction) solution for $C$:

$$C = \tanh(\frac{x}{\sqrt{2}\varepsilon}) \tag{2.7}$$

The interface width $L_c$ is defined as the distance from $C$ = -0.9 to $C$ = 0.9, so $L_c \approx 4.164\varepsilon$. This diffuse interface with a certain physical sense is the key characteristic of phase-field model. Choosing an appropriate value of $\varepsilon$ and an adequate grid resolution for $L_c$ is precondition of reliable simulations.

Evolution of $C$ is described by the Cahn-Hilliard (CH) equation through approximating interfacial diffusion to be proportional to chemical potential gradient:

$$\frac{\partial C}{\partial t} + (\vec{u} \cdot \nabla) C = \kappa \nabla^2 \phi \tag{2.8}$$

here $t$, $\vec{u}$, and $\kappa$ denote time, velocity field and mobility, respectively. The term on the right side is a diffusive term, which allows the contact lines to move at a solid wall, in combination with the no-slip boundary. In order to accurately model the motion of contact lines, an appropriate value of $\kappa$ needs to be chosen.

Based on the wall free energy formulation at local equilibrium, the boundary condition for parameter $C$ on the bottom wall can be described as follows with contact angle $\theta$ [39]:

$$\vec{n_s}\cdot \nabla C = \frac{\sqrt{2}}{2}\frac{\cos(\theta)}{\varepsilon}(1-C^2) \tag{2.9}$$

where $\vec{n_s}$ and $\varepsilon$ indicate normal vector of the wall and capillary width, respectively.

In this study, two-phase flow of immiscible, incompressible, isothermal and Newtonian fluids is considered. The single-field Navier-Stokes (NS) equation describes the fluid flow.

$$\nabla\cdot \vec{u} = 0 \tag{2.10}$$

$$\frac{\partial}{\partial t}(\rho_c\vec{u}) + \nabla\cdot(\rho_c\vec{u}\otimes\vec{u}) = -\nabla p + \nabla\cdot[\mu_c(\nabla\vec{u} + (\nabla\vec{u})^T)] + \vec{f_\sigma} + \rho_c\vec{g} \tag{2.11}$$

where $p$, $\vec{g}$, $\vec{f_\sigma}$ are pressure, gravitational acceleration and interfacial force. The interfacial force is defined as [14]:

$$\vec{f_\sigma} = -C\nabla\phi \tag{2.12}$$

The density and viscosity are dependent on order parameter $C$:

$$\rho_c = \frac{1+C}{2}\rho_l + \frac{1-C}{2}\rho_g \tag{2.13}$$

$$\mu_c = \frac{1+C}{2}\mu_l + \frac{1-C}{2}\mu_g \tag{2.14}$$

where subscript $l$ and $g$ indicate liquid and gas phase, respectively.

### 2.2.2. Discussion of Phase-field Parameters

In the present study, droplets of diameters ranging from 0.01 mm to 3 mm are simulated. The physical interface thickness is, however, typically on the scale of tens of nanometers. The disparity in the order of magnitude between both scales can be up to 5. Simultaneously resolving both scales is computationally unaffordable. Since the global features of droplets are of our interest, an artificially thicker interface needs to be used. In order to determine the value of capillary width $\varepsilon$, a dimensionless number, Cahn number $Cn = \varepsilon/L$ is introduced, which is defined as the ratio between capillary width $\varepsilon$ and reference length $L$. To choose an appropriate value of $Cn$, the numerical accuracy, efficiency and stability must be considered [39]. For a droplet, the reference length equals diameter $D$. From the experience of researchers [7, 17, 39, 8], if $\varepsilon$ is chosen so that $Cn \leq 0.01 \sim 0.02$, the simulation results are then insensitive to $\varepsilon$.

The overall accuracy of the method is also affected by mesh spacing $h$. A dimensionless number $Nc = L_c/h$ is defined as the ratio between interface width $L_c$ and mesh spacing $h$. Both $Nc$ and $Cn$ decide on the degree of details we can obtain for phenomena at the local contact line region [7]. To capture the local features more accurately, choosing a small $Cn$ and a large $Nc$ is necessary. In chapter 3, the sensitivity studies to $Nc$ and $Cn$ are carried out.

Another important parameter inherent to phase-field method is the mobility factor $\kappa$. It quantifies the diffusive process of contact line motion on the wall, according to equation 2.8. Since the diffusion is essentially on molecular scale, a direct resolution onto it is impossible. A first estimate of the value of $\kappa$ is $\kappa \propto O(\varepsilon^2)$. In this case, $\kappa$ and the CH diffusion goes to zero as $\varepsilon$ approaches zero. The sharp interface model is therefore recovered by phase-field model [14]. $\kappa$ is determined by comparing with the experimental

or analytical data, since it can be regarded as a material intrinsic property of a certain physical system [44].

### 2.2.3. Numerical Methodology

All of the simulations in the present study are performed on the platform OpenFOAM® (for "Open Source Field Operation And Manipulation"), which is a free and open source C++ toolbox for solving continuum mechanics problems, including computational fluid dynamics (CFD). The solver used in the simulations is $phaseFieldFoam$, which is developed and implemented by Marschall and Cai [27, 28]. The solution procedure of CH equation and NS equation from time step $n$ to $n+1$ is described as follows:

1. Calculate the chemical potential $\phi(t_n)$ by equation 2.5 using $C(t_n)$.
2. Obtain $C(t_{n+1})$ by solving CH equation 2.8 by using $\phi(t_n)$ and $\vec{u}(t_n)$.
3. Obtain $\phi_(t_{n+1})$, $\rho_c(t_{n+1})$, $\mu_c(t_{n+1})$ using $C(t_{n+1})$ and then, calculate $f_\sigma(t_{n+1})$ by equation 2.12 by using $\phi(t_n)$, $\phi_(t_{n+1})$ and $C(t_{n+1})$.
4. Obtain $\vec{u}(t_{n+1})$ by NS equations 2.10 and 2.11.

By using this solution procedure together with the given initial and boundary conditions, the CH and NS equation system can be solved.

# 3. Study of Single Droplet Impact and Rebound

The chapter reports three validations for a single droplet concerning spread factor and morphology evolution, maximal spread factor and contact time with the wall. After the validations, the impact behavior of a single AdBlue droplet is investigated. Since all the cases studied in this chapter are physically symmetric problems, 2D axisymmetric simulations are conducted to save the computational costs.

## 3.1. Validation 1: Spread Factor and Morphology Evolution

In this section, an experiment from literature is selected for the validation concerning spread factor and morphology evolution. The numerical parameters are firstly determined. Then, the results of simulations are compared with the experiment.

### 3.1.1. Physical Properties and Computational Setup

The experiment was conducted by Zang et al. [46]. In the experimental setup, a water drop with 2 wt% Wacker H30 silica nanoparticles impacted on a superhydrophobic surface with dendrite structure. By controlling the falling height, the impact velocity was set as 0.63 m/s. The diameter of the drop was 2.67 mm, the contact angle was 163°and the surface tension between the liquid and gas phases was 71.6 mN/s. The fluid properties were globally similar as water.

In the present simulations, the wall is ideally smooth and homogeneous. The diameter of the drop, the impact velocity and contact angle are set up the same as the experiment. For the drop and the surrounding gas, water and air are used, and the physical properties of the two phases are listed in Table 3.1.

Table 3.1.: Physical properties of the fluids.

| | Density $\rho$ [kg/m$^3$] | Viscosity $\nu$ [m$^2$/s] | Surface tension $\sigma$ [ mN/m] |
|---|---|---|---|
| Water | 998.21 | $1.004 \cdot 10^{-6}$ | 72.75 |
| Air | 1.188 | $1.535 \cdot 10^{-5}$ | |

The computational domain (see Figure 3.1 (a)) for the 2D axisymmetric simulation consists of a solid wall under the drop, empty-type planes on the two sides and free stream edges. This domain is discretized by a stationary, structured and uniform grid

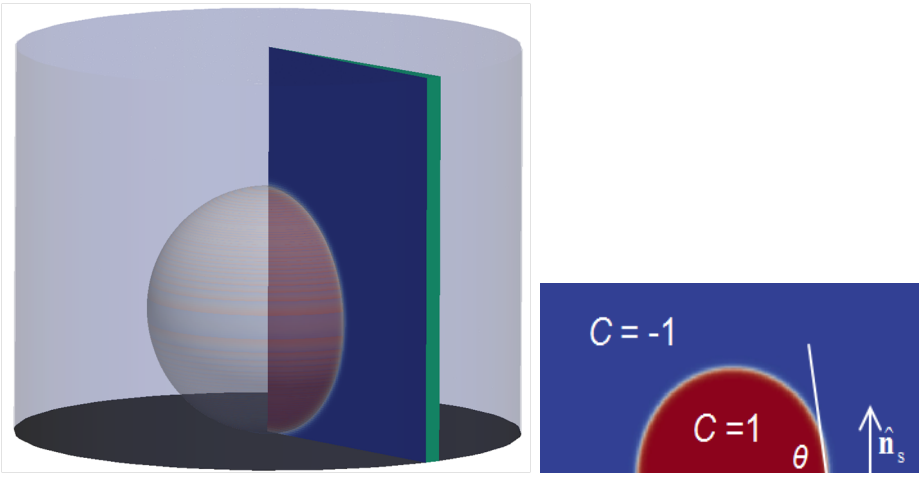


(a) Computational domain. Taken from [2]. (b) Boundary conditions for $C$.

Figure 3.1.: Computational domain and boundary conditions.

with mesh size $h$ so that the interface width and the initial drop diameter is resolved by $Nc = L_c/h$ und $N_d = D_0/h$ mesh cells ($L_c$ is here interface width and $D_0$ is initial droplet diameter). The boundary conditions for the Navier-Stokes equations are set as $pressureInletOutletVelocity$ with zero pressure gradient at the top and bottom of the computational domain, no-slip condition for velocity on the bottom wall. Zero gradient conditions are used for Cahn-Hiliard equation except for the bottom wall (see Figure 3.1 (b)). The boundary condition for parameter $C$ on the bottom wall is set according to Equation 2.9.

The simulation is started from an initially spherical drop (diameter $D_0$), whose center point lies above the wall with the height of $D_0/2$ (see Figure 3.1 (a)). All of the cells inside the drop ($C \geq 0$ ) are initialized with the impact velocity. The interface is initialized by using Equation 2.7 in 2D expression.

### 3.1.2. Numerical Parameter Study

Three important numerical parameters (mesh resolution $Nc$, Cahn number $Cn$ und mobility factor $\kappa$) are studied to determine an optimal combination of them.

Firstly, grid sensitivity analysis is conducted to quantify the effect of mesh resolution. The simulations are carried out with different mesh resolutions. Figure 3.2 shows the time evolution of the spread factor $\beta$ with $Nc = 2$, 4, 6 and 8, respectively. The Cahn number $Cn = 0.02$ and mobility factor $\kappa = 2.8 \cdot 10^{-9}$ m$^3$s/kg are kept constant. It is found that, the numerical results are insensitive on $Nc$, when $Nc \geq 6$. The interface width is therefore resolved by at least six mesh cells.

Then, keeping mesh resolution $Nc = 6$ and mobility factor $\kappa = 2.8 \cdot 10^{-9}$ m$^3$s/kg, the influence of Cahn number $Cn$ is studied. Figure 3.3 shows the simulation results for $Cn$ = 0.01, 0.02, 0.04 and 0.08, respectively. It is interesting to observe that, as $Cn$ decreases to 0.02, the results are converging for the most of the process. For $Cn = 0.01$, at the beginning of the impact process (at time of 0.8 ms in the Figure 3.3), there exists air entrapment, which causes an early rebounce of the drop. Since this phenomenon was not reported in the experiment of Zang et al. [46], and we are concerned about the global evolution of the drop, this phenomenon is not further investigated in this part. Thus, $Cn$ = 0.02 is selected. The air entrapment is further discussed in Figure 3.15.

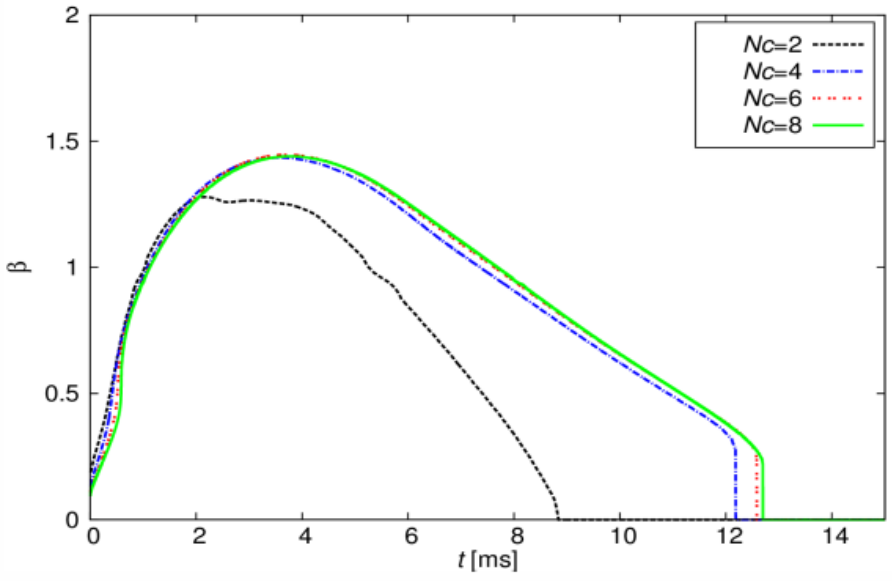


Figure 3.2.: Influence of mesh resolution on time evolution of spread factor. $Cn = 0.02$ and $\kappa = 2.8 \cdot 10^{-9}$ m$^3$s/kg.

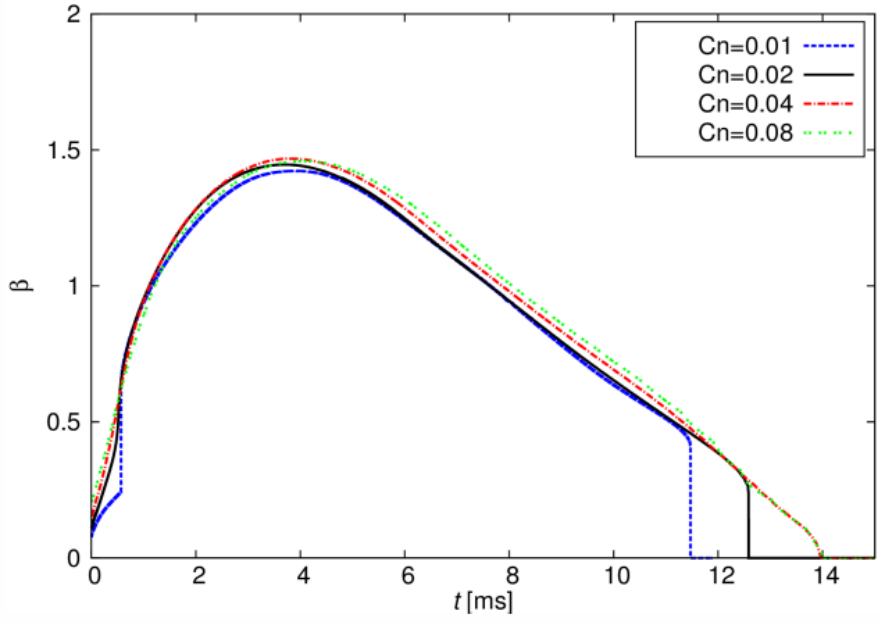


Figure 3.3.: Influence of Cahn number on time evolution of spread factor. $Nc = 6$ and $\kappa = 2.8 \cdot 10^{-9}$ m$^3$s/kg.

At last, the mobility factor $\kappa$ is studied. Here $Cn = 0.02$ and $Nc = 6$ are fixed. $\kappa$ is usually treated as a phenomenological parameter and is determined through fitting with experiment. The first estimate of the value of $\kappa$ is that, $\kappa = O(\varepsilon^2)$. Around this estimate value, $\kappa$ is varied and finally chosen by fitting with experimental data. Figure 3.4 shows the simulation results with $\kappa = 1 \cdot 10^{-10}$, $5 \cdot 10^{-10}$, $25 \cdot 10^{-10}$, $125 \cdot 10^{-10}$ m$^3$s/kg and the experimental data. As $\kappa = 25 \cdot 10^{-10}$ m$^3$s/kg and $\kappa = 125 \cdot 10^{-10}$ m$^3$s/kg , the drop rebounds earlier than in the experiment. This is reasonable since the contact line is driven by diffusion in the phase-field method [6]. Thus, a larger mobility factor, i.e., a stronger diffusion leads to a faster spreading and therefore earlier occurrence of rebound.

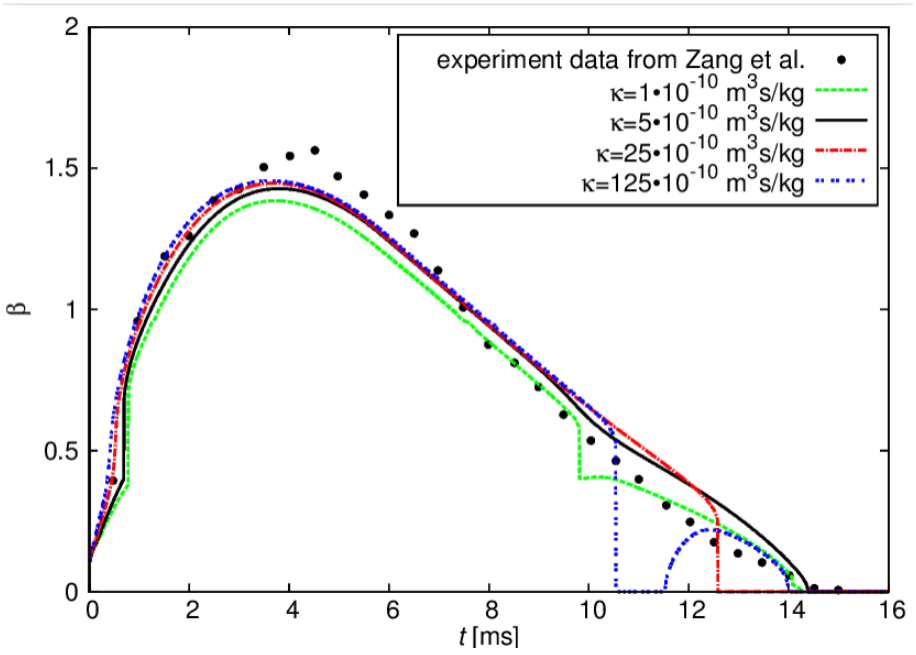


Figure 3.4.: Influence of mobility factor on time evolution of spread factor. $Cn = 0.02$ and $N_c = 6$.

As $\kappa = 1 \cdot 10^{-10}$ m$^3$s/kg , the bubble beneath the drop has an influence on the result, which is indicated in the figure at the time of $t = 9.8$ ms. The simulation result with $\kappa = 5 \cdot 10^{-10}$ m$^3$s/kg has a good agreement with the experimental data. $\kappa = 5 \cdot 10^{-10}$ m$^3$s/kg is therefore used in the subsequent simulations.

### 3.1.3. Comparison with Experimental Results for Morphology Evolution

The droplet morphology evolution predicted by the simulation with $Nc = 6$, $Cn = 0.02$ and $\kappa = 5 \cdot 10^{-10}$ m$^3$s/kg is compared with that recorded in the experiments. This is displayed in Figure 3.5.

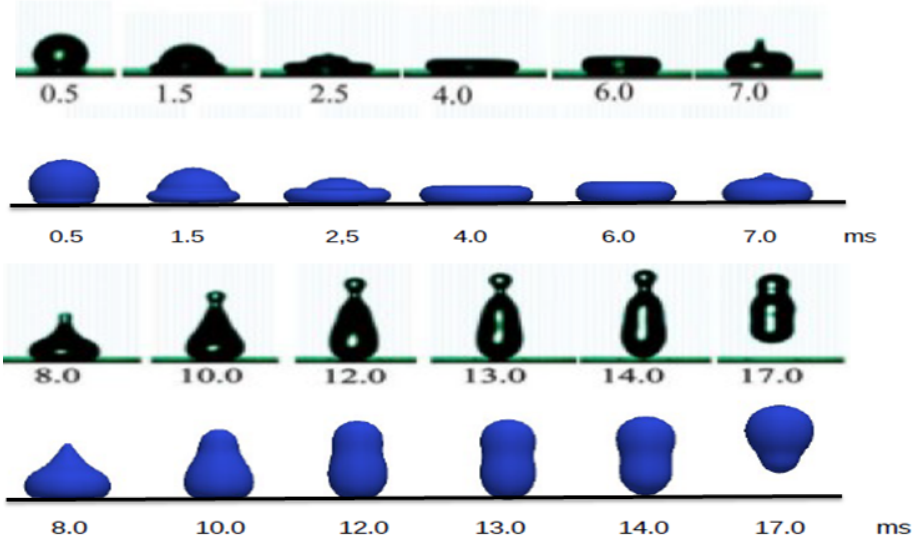


Figure 3.5.: Time evolution of the droplet shape from side view. The first and third rows with black droplets indicate the experimental result [46]. The second and last rows with blue ones illustrate the present numerical result.

The initial spreading is mainly driven by the kinetic energy ($t \leq 4$ ms), and at $t = 4$ ms, the droplet spreads to its maximum length and then begins to recoil due to the conversion of surface energy into kinetic energy ( $t > 4$ ms). The droplet bounces off the surface at $t \approx 14$ ms because of enough total kinetic energy. The numerical result matches the experimental result very well from the beginning until $t = 8$ ms. After this time a narrow neck near the top of the drop appeared in the experiment, which can not be captured in the simulation. The reason is that in the experiment of Zang et al. [46], water with silica nanoparticles was used, which shows non-Newtonian characteristics in local areas. In the present simulation, however, Newtonian fluids are assumed.

The drop volume conservation is illustrated in Figure 3.6. The drop volume is calculated through the integration of the surface area where order parameter $C > 0$. The order parameter $C$ ranges from -1.00017 to 1.00444. One can find that the volume conservation (based on volume $C > 0$) is very good during the whole process.

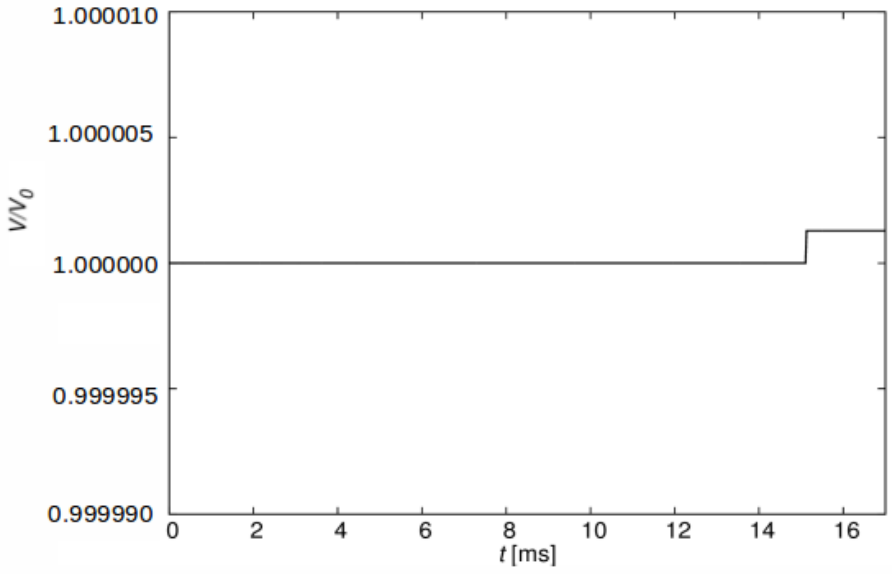


Figure 3.6.: Drop volume conservation in the simulation. $V_0$ is initial drop volume and $V$ is instantaneous drop volume.

## 3.2. Validation 2: Maximal Spread Factor

Scheller et al. [36] have correlated the maximal spread factor with the dimensionless group $Re^2Oh$ through glycerin-water drop impact experiments:

$$\beta_{\max} = 0.62(Re^2Oh)^{0.166} \tag{3.1}$$

The experimental data is as follows: liquid viscosity is 1-300 mPas, liquid surface tension 40-73 mN/m, contact angle 35-90°, drop diameters 2.0-4.0 mm, and impact velocities 1.30-4.90 m/s. The liquid density was varied with glycerin content by 10%. The $Re$ and $Oh$ numbers ranged from 19 to 16400 and from 0.0020 to 0.58, respectively.

In the present simulations, water drops are used and the physical properties are kept constant. The drop diameters range from 0.05 to 0.8 mm, impact velocities range from 5 to 10 m/s, leading to $Re$ range from 357 to 2858 and $Oh$ from 0.0060 to 0.034. The simulations are carried out under three different contact angles, i.e. 30°, 95° and 130°. Numerical parameters are set as: $Nc = 6$, $Cn = 0.02$, $\kappa/\varepsilon^2 = 1$ ms/kg.

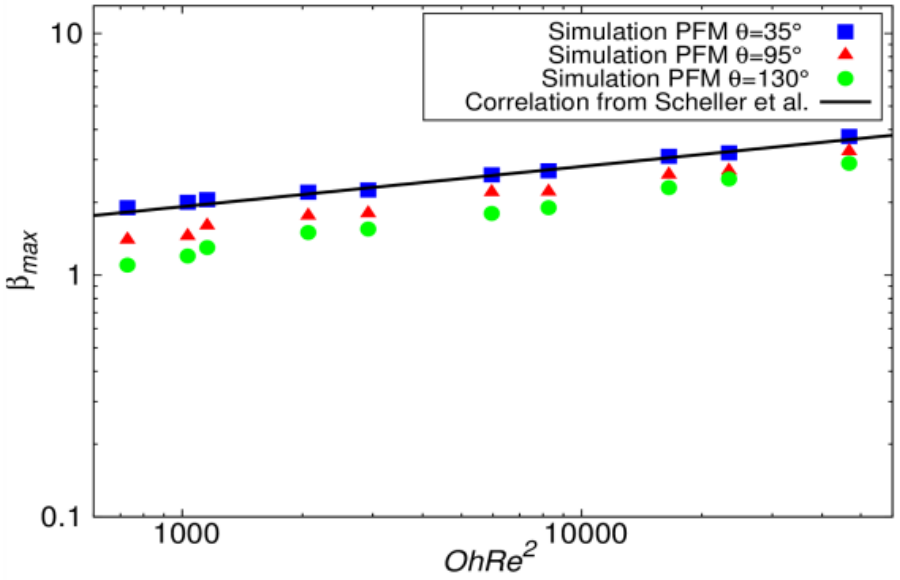


Figure 3.7.: Maximal spread factor correlated against $Re^2Oh$.

Figure 3.7 shows the comparison of the numerical results with the experimental correlation. One finds an excellent agreement between the numerical results under the contact angle 35° and the correlation. For the two other contact angles, the maximal spread factor of the correlation is underpredicted by the simulations especially for the low $Re$ and $Oh$. This indicates that, the contact angle has significant influence on the maximal spread factor for the low $Re$ and $Oh$. This influence becomes smaller as $Re$ and $Oh$ increase. This can be substantiated by Rioboo et al. [32], who have also stated that, the maximal spread factor only slightly depends on the wettability of the substrate if the impact $Re$ and $We$ are high. The study of Antonini et al. [1] has also shown that, for a millimetric drop impacts at $We$ lower than 200, the maximal spread factor and spreading time are both influenced by surface wettability, while for high $We$, the effect of wettability is negligible since inertial effects dominates the capillary effect. This trend can also be simply understood that, the surface wettability becomes important only when the contact line moves slowly, since only under this situation do the adhesion forces start to play a role [26].

## 3.3. Validation 3: Contact Time with the Wall

Further validation of the single drop impact is performed for the contact time $T_c$ (i.e., time between impact and rebound instants, see Figure 3.8 ). This problem was originally

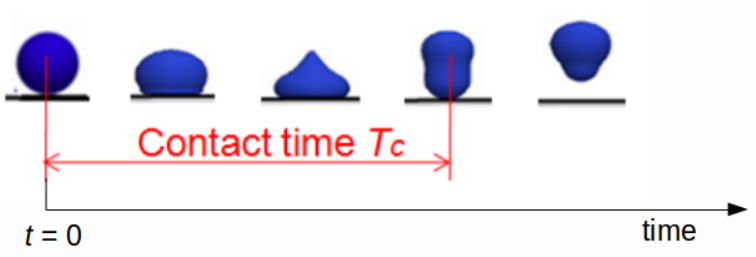


Figure 3.8.: Time evolution of the droplet shape. The first and fourth picture indicate the impact and rebound instant, respectively. $T_c$ is contact time.

studied by Richard et al. [32]. In the experiment, water droplets with radii ranging from 0.1 to 4 mm were impinged on a superhydrophobic surface. The impact velocity ranged from 0.2 to 2.3 m/s. They have found out that the contact time does not depend on the impact velocity over this range of velocities. The contact time is mainly determined by the drop radius ($T_c \sim R^{3/2}$). This finding can be simply explained. By balancing inertia $\rho R/t^2$ with capillary $\sigma/R^2$, we obtain contact time $T_c = (\rho R^3/\sigma)^{1/2}$, which is the same as the scaling for the first-order vibration period of a freely oscillating drop derived by Rayleigh [31] (the so-called Rayleigh time or drop free oscillation time, which equals to $\pi/\sqrt{2}(\rho R^3/\sigma)^{1/2}$). According to Watchers and Westerling [40], similar formula was also obtained for drop impacting on a hot surface in Leidenfrost conditions.

In the present simulations, the drop radii range from 0.05 to 0.8 mm, impact velocities are in the range of 1 to 3 m/s. The properties of fluids are the same as that of the experiment. Numerical parameters are set as: $Nc = 6$, $Cn = 0.02$, $\kappa = 4 \cdot 10^{-12}$, $16 \cdot 10^{-12}$, $64 \cdot 10^{-12}$, $256 \cdot 10^{-12}$ m$^3$s/kg (for radii 0.05, 0.1, 0.2, 0.4 mm, respectively). In Richard et al. [32], the precise value of contact angle was not given, thus the influence of contact angle on the contact time is firstly investigated. As illustrated in Figure 3.9, the contact time decreases with the increasing contact angle, but the decrease rate is sinking. The contact time decreases only slightly when the contact angle greater than 170°. The contact angle is therefore set as 170° in the simulations.

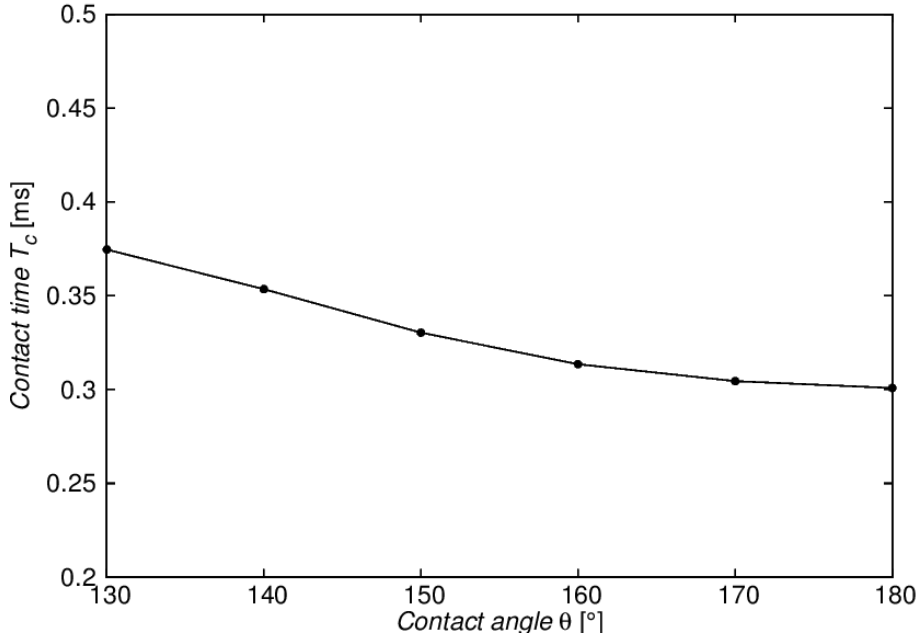


Figure 3.9.: Influence of contact angle on the contact time. Droplet diameter $D = 0.2$ mm, impact velocity $U = 2$ m/s.

Then, the first finding of Richard et al. [32] is used to validate the present numerical method. As shown in Figure 3.10 the simulations confirm the independence of the contact time on the impact velocity, which was reported in the study of Richard et al. [32].

Another important finding of Richard et al. [32] was the correlation of $T_c$ with $\rho$, $\sigma$ and $R$:

$$T_c = 2.6 \left(\frac{\rho}{\sigma}\right)^{1/2} R^{3/2} \tag{3.2}$$

where $\rho$, $\sigma$ and $R$ are density, surface tension and drop radius, respectively. The prefactor 2.6 was deduced from experiment, which is greater than that of the Rayleigh time. This correlation is used to validate the present numerical method. In Figure 3.11, the red

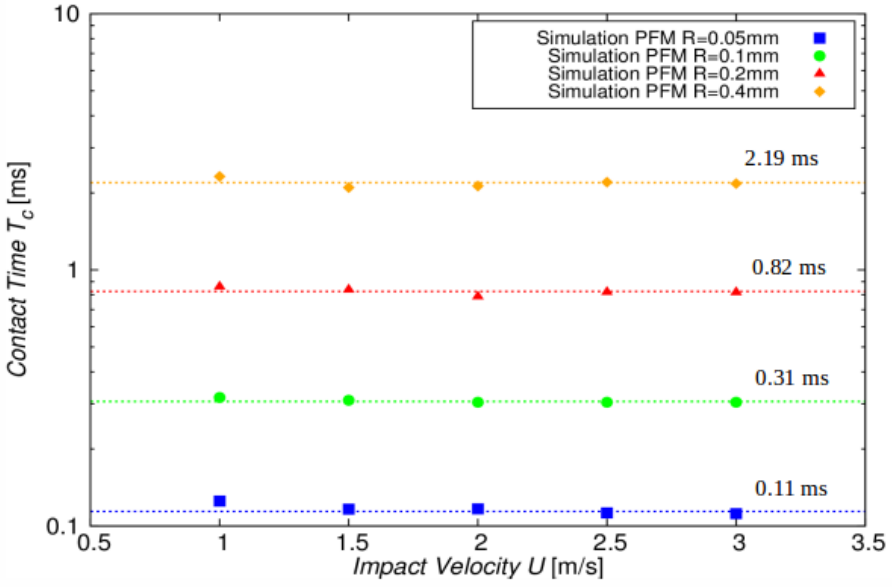


Figure 3.10.: Contact time of bouncing drops with different radii. The different lines indicate the average contact time. Contact angle $\theta = 170^o$.

triangles and blue squares are the experimental data from Richard et al. [32] and the present simulation results, respectively. The black line is the correlation. In this figure, a good agreement of the numerical results with the correlation can be observed. The reason why the contact time of larger droplets is slightly shorter than that of the correlation is that the bubble entrapment exists more easily for larger droplets. This bubble entrapment can lead to an earlier rebound.

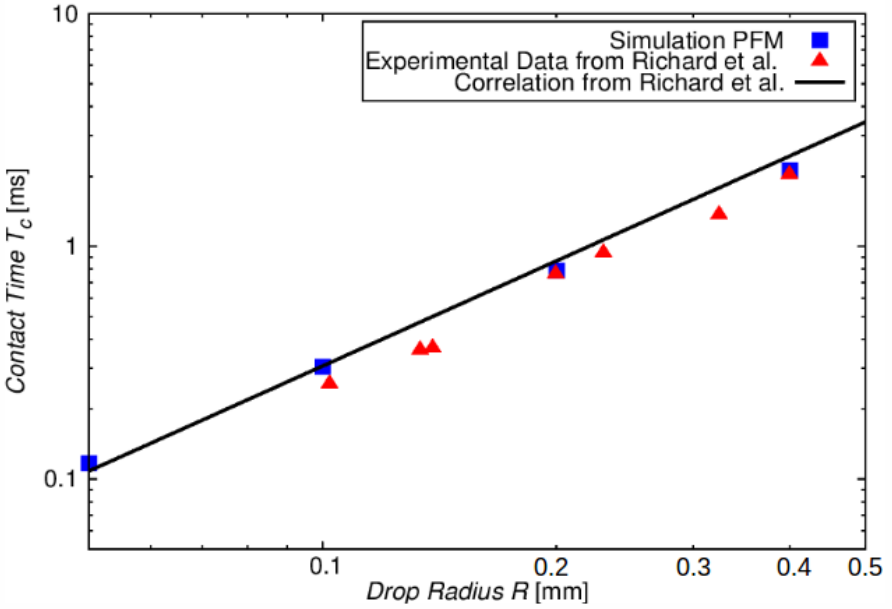


Figure 3.11.: Contact time of a bouncing drop as a function of drop radius. Contact angle of the present simulation $\theta = 170^o$.

## 3.4. Study of the Impact Behavior of a Single AdBlue Droplet

In this section, the impact behavior of a single AdBlue droplet under different conditions is studied. Deposit and rebounce phenomena are focused. Firstly, the influence of the physical parameters (contact angle $\theta$, impact velocity $U$, droplet diameter $D$) are respectively investigated. The physical properties and parameters of the AdBlue droplets used in the simulations are listed in Table 3.2. The simulation results are then presented with regime maps for different dimensional parameters. At last, regime maps for dimensionless parameters are generated in order to compare the numerical results with experimental data and theoretical model from literature.

Table 3.2.: Parameters for AdBlue droplet simulations.

| Items | Values or range |
|---|---|
| Density $\rho$ [kg/m$^3$] | 1090 |
| Kinematic viscosity $\nu$ [m$^2$/s] | $1.4 \cdot 10^{-6}$ |
| Surface tension $\sigma$ [mN/m] | 73.26 |
| Contact angle $\theta$ [°] | 50-180 |
| Impact velocity $U$ [m/s] | 0.01-10 |
| Droplet diameter $D$ [mm] | 0.01-0.8 |

### 3.4.1. Effects of Physical Parameters

The results in Figure 3.12-3.14 comprise the spread factor $\beta$ of a droplet as functions of time from impact under different conditions.

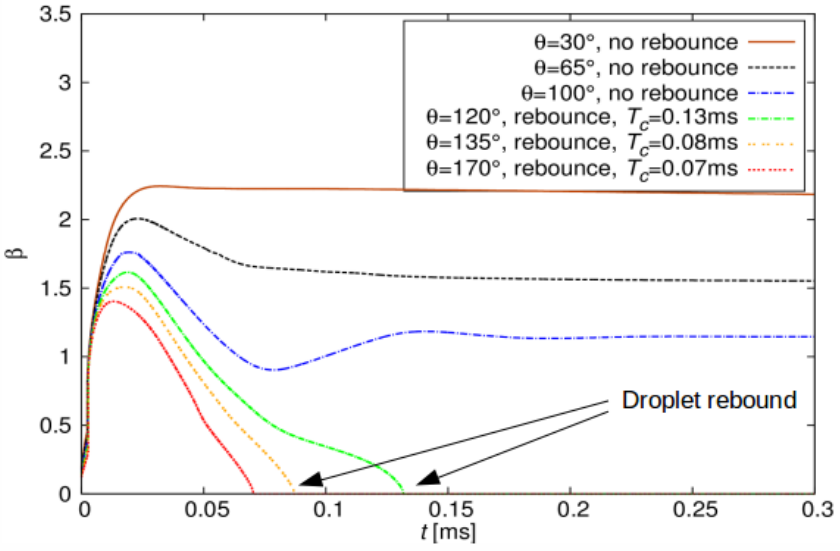


Figure 3.12.: Influence of contact angle on droplet behavior. $D = 0.0683$ mm, $U = 7.228$ m/s. $T_c$ is contact time. (see Figure 3.8.)

Figure 3.12 shows the effect of contact angle on the impact process of a 0.0683 mm AdBlue droplet. The impact velocity is fixed as 7.228 m/s and the contact angle ranges from 30° to 170°. At the very beginning, the contact angle has no effect on the impact process. After $t$= 0.01 ms, there is significant difference among the curves for different contact angles. Rioboo et al. [33] have also stated that, the wettability has no influence

during the kinematic phase, but in the following stage its effect can be important. The maximum spread factor increases with decreasing contact angle. Another trend is that, the droplet with larger contact angle reaches the maximum spread factor earlier. Moreover, the droplet is easier to rebound from the wall with larger contact angle, since more hydrophobic surface with large contact angle will more energetically repel the droplet. In Figure 3.12, one can observe that the droplet rebounds as the contact angle equals 120°, 135° or 170° (at the time $t$= 0.13, 0.08 and 0.07 ms, respectively), while it deposits as contact angle is 30°, 65° or 100°.

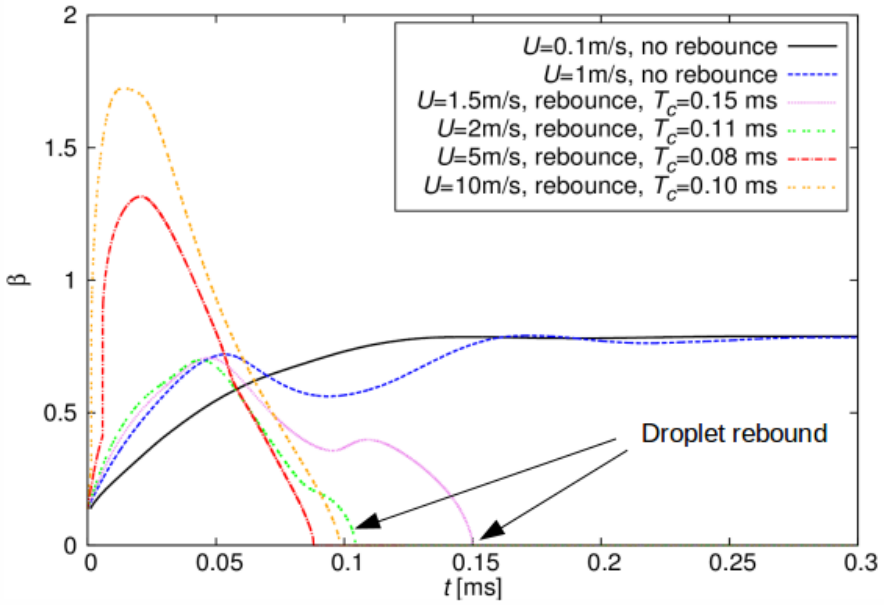


Figure 3.13.: Influence of impact velocity on droplet behavior. $D = 0.0683$ mm, $\theta = 130°$. $T_c$ is contact time.

Figure 3.13 presents the influence of impact velocity. The 0.0683 mm AdBlue droplet impacts on the wall with the contact angle of 130°. The impact velocity has influence on the whole impact process. Increasing the impact velocity leads to faster spreading. The tendency of rebounce increases with increasing impact velocity within this range. If the impact velocity is high enough, the droplet can then rebound. Figure 3.13 illustrates that the droplet rebounds with the impact velocities of 1.5, 2, 5 and 10 m/s, while it deposits with the impact velocities of 0.1 and 1 m/s. For a small impact velocity, the droplet immediately sticks to the surface and the kinetic energy is dissipated out by viscous force. The droplet can not bounce back because there is no enough kinetic energy left. If the impact velocity is high enough, i.e., the initial kinetic energy is sufficiently large, so that the droplet can then rebound.

Figure 3.14 shows the impact processes of droplets with diameters of 0.1, 0.2, 0.4 and 0.8 mm, respectively. The impact velocity is fixed as 5 m/s and the contact angle kept as 130°. The maximum spread factor is reached earlier for the smaller droplet, but the value of it is lower than that of the larger one. Obviously one can also see that the smaller droplet rebound much earlier. This suggests that the time scale of the impact process is much dependent on the size of the droplet. At $t \approx 1.6$ ms, the spread factor of the 0.8 mm droplet decreases suddenly to zero, which is due to the formation of air film beneath the droplet (see Figure 3.15).

Apart from the spread factor, the dimensionless maximum rebound height $H_{\max}/D$ also indicates the impact dynamics ($H_{\max}$ is here maximum rebound height, $D$ is droplet

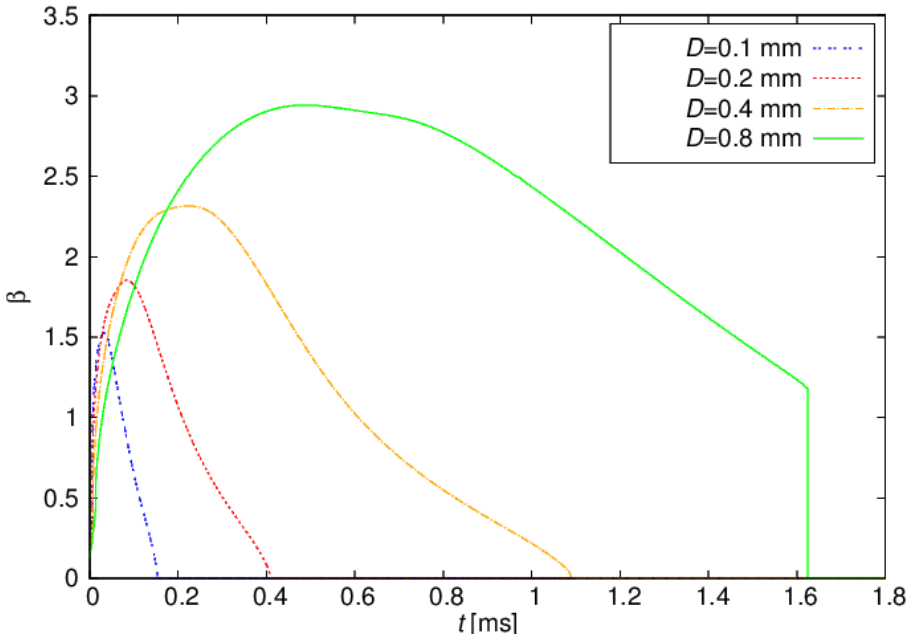


Figure 3.14.: Influence of diameter on droplet behavior. $\theta = 130^{o}$, $U = 5$ m/s.

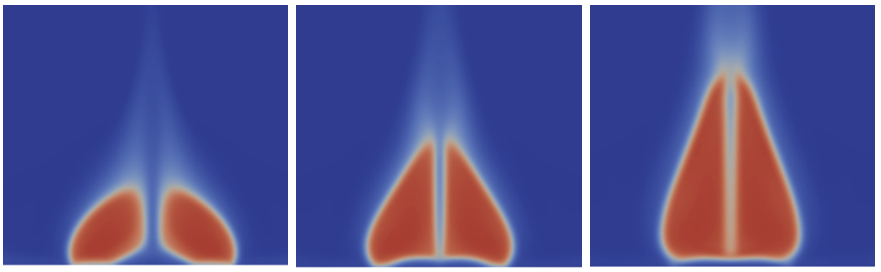

(a) $t = 1.5$ ms. (b) $t = 1.6$ ms.. (c) $t = 1.7$ ms..

Figure 3.15.: Air film beneath the droplet with diameter of 0.8 mm around $t = 1.6$ ms.

diameter). Figure 3.16 demonstrates the dimensionless maximum rebound height of a 0.0683 mm AdBlue droplet under different contact angles and impact velocities. The contact angles range from 120° to 180° and the selected impact velocities are 1, 3, 5, 7 m/s. Under the same impact velocity, the maximum rebound height increases as the contact angle is greater. The increasing rate of the maximum rebound height is, however, decreasing with the increasing contact angle. One can observe that the maximum rebound heights under the contact angle of 170° and 180° are almost the same. Under the same contact angle, the relation of the maximum rebound height and impact velocity is complex. As the contact angle greater than 140° (in the region of superhydrophobic), the increase of impact velocity leads to greater maximum rebound height. As contact angle ranges from 120° to 140°, the maximum rebound height has no monotonous relation with the impact velocity. This phenomenon is due to the interaction between the capillary and inertial effects.

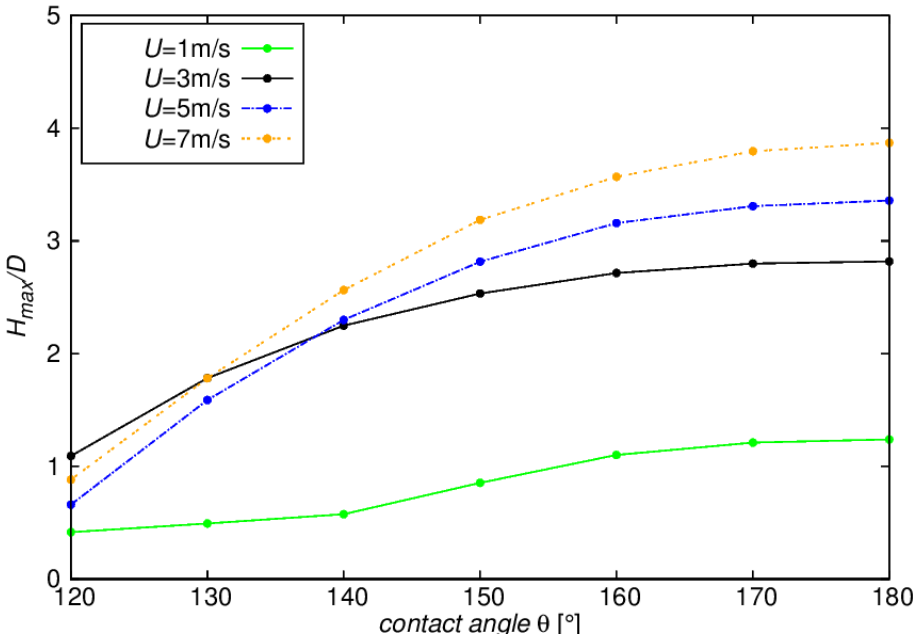


Figure 3.16.: Influence of contact angles and impact velocities on dimensionless maximum rebound height. Droplet diameter $D = 0.0683$ mm.

### 3.4.2. Regime Maps for Physical Parameters

In order to understand the details of the combined effects of the three physical parameters studied in Section 3.4.1., a large number of simulations are performed through systematically changing these parameters. Three regime maps are therefore generated, and are respectively illustrated in Figure 3.17, 3.18 and 3.19. In these figures, each symbol represents one simulation case. Simulations where rebound is observed are marked by red triangles and cases with deposition are indicated by blue squares.

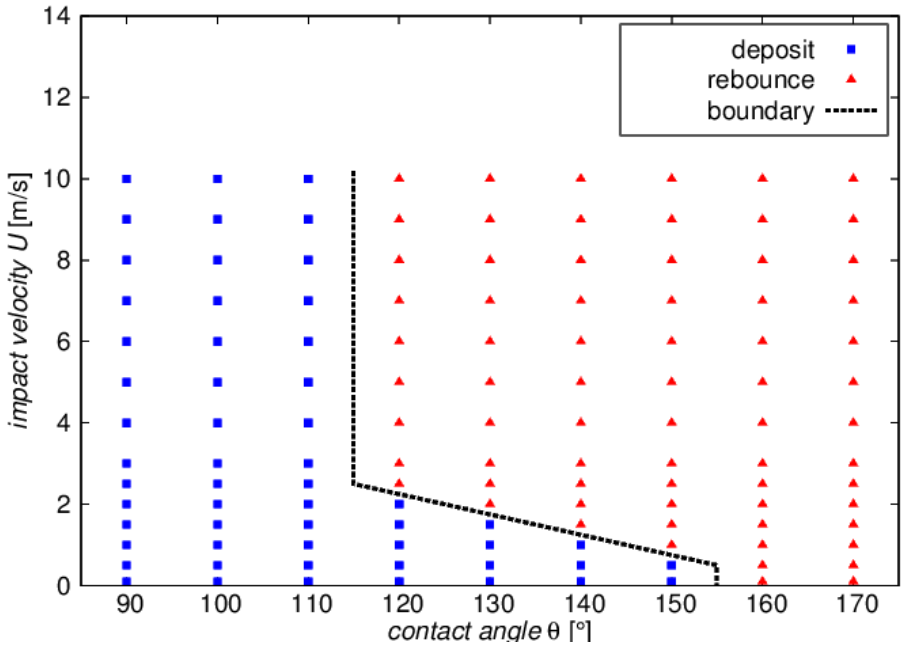


Figure 3.17.: $\theta - U$ regime map. $D = 0.0683$ mm.

In Figure 3.17, the contact angle and impact velocity are varied in the range from

90° to 170° and from 0.01 to 10 m/s, respectively. The droplet diameter is fixed as 0.0683 mm. The rebounce-zone is characterized by larger contact angle and higher impact velocity, while the deposit-zone corresponds to the cases where both the quantities are small. The threshold values of impact velocity and contact angle exist for the transition from deposit-zone to rebounce-zone. As contact angle increases, the threshold value of impact velocity decreases. The contact angle characterizes the wettability of the wall and a larger contact angle shows a property of water repellency, and the droplet is thus easier to rebound from the wall.

In Figure 3.18, a regime map is generated for different droplet diameters and impact velocities. The droplet diameters range from 0.01 to 0.8 mm and the impact velocities from 0.5 to 3 m/s. Contact angle is kept as 130°. The rebounce-zone lies above the deposit-zone and the boundary between the two regimes can be clearly recognized. In this figure, one can find that droplet with larger impact velocity or larger diameter is easier to rebound in this studied domain. This is mainly due to the larger kinetic energy.

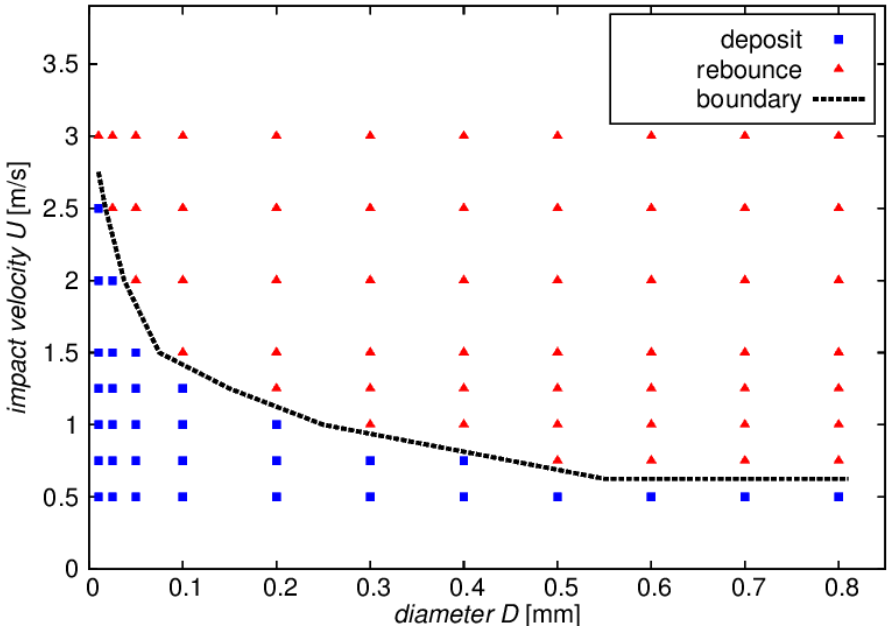


Figure 3.18.: $D - U$ regime map. $\theta = 130°$.

In Figure 3.19, the droplets with the impact velocity of 7.228 m/s are simulated. The droplet diameters and contact angles range from 0.01 to 0.4 mm and from 90° to 130°, respectively. Here, one observes that, when contact angle $\theta \leq 105°$, the droplet deposits, while the droplet rebound when the contact angle $\theta \geq 120°$. As $105° < \theta < 120°$, non-monotonousness is found when the droplet diameter $R$ increases from 0.01 to 0.4 mm. For the contact angle $\theta = 110°$, droplets with diameter $D = 0.01$ mm or $D \geq 0.2$ mm can rebound, while the ones with diameter 0.02 mm $\leq D \leq 0.1$ mm deposit. This complex transition mechanism is due to the interaction between the inertial, viscous and capillary forces and a further investigation is needed.

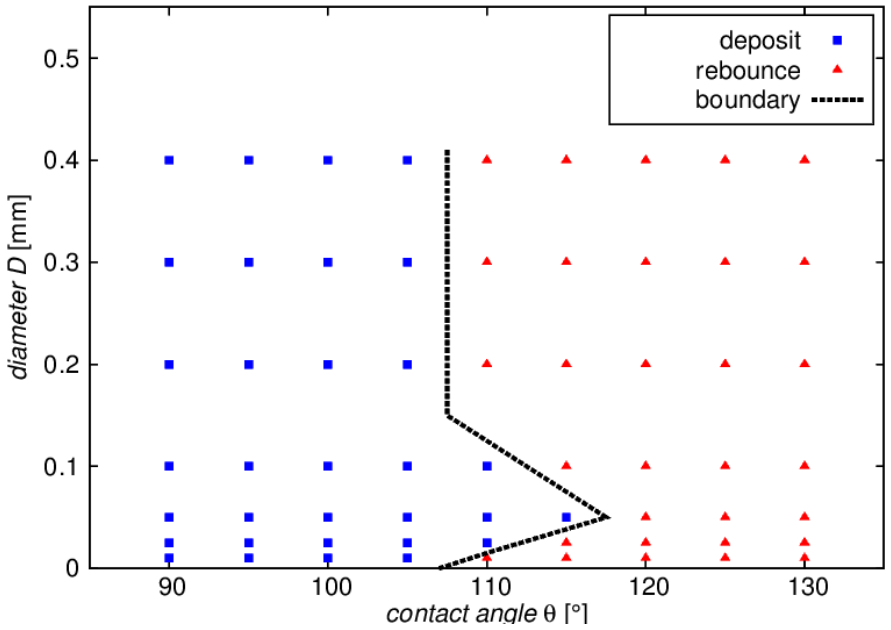


Figure 3.19.: $\theta - D$ regime map. $U = 7.228$ m/s.

### 3.4.3. Regime Maps based on Dimensionless Parameters

In order to deeply understand the mechanisms of deposit-rebounce transition, regime maps are generated for dimensionless parameters. Here, the numerical results are compared with reference data from literatures. In the literature of Rioboo et al. [35], four outcomes have been identified, i.e., deposit, rebounce, sticking and fragmentation. Here only the experimental data for the situation of deposit and rebounce is selected to make the comparison. The experiment were carried out at various impact speeds (0.017-7.17 m/s) and with various drop diameters (93 $\mu$m to 4.72 mm) on a superhydrophobic surface with contact angle of 150°. Since the contact angle is fixed, the influence of wettability is here not studied. But other important factors such as viscosity, surface tension, drop diameter and impact velocity can be through $Re$ and $We$ considered. In our simulation, $Re$ varies from 100 to 700 and $We$ from 0.02 to 4.

In Figure 3.20, the rebounce and deposit regimes are presented with red triangles and blue squares, respectively. The filled and hollow symbols indicate the simulation results and experimental data of Rioboo et al. [35], respectively. A good agreement can be observed. The rebounce-zone is characterized by large $We$. When $Re$ is constant, the droplet rebounds at high $We$ and deposits at low $We$. This suggests that the transition from deposit to rebounce is governed by $We$. It was proposed by Rioboo et al. [35] that the transition depends on $We$ and the solid surface parameters (contact angle and contact angle hysteresis).

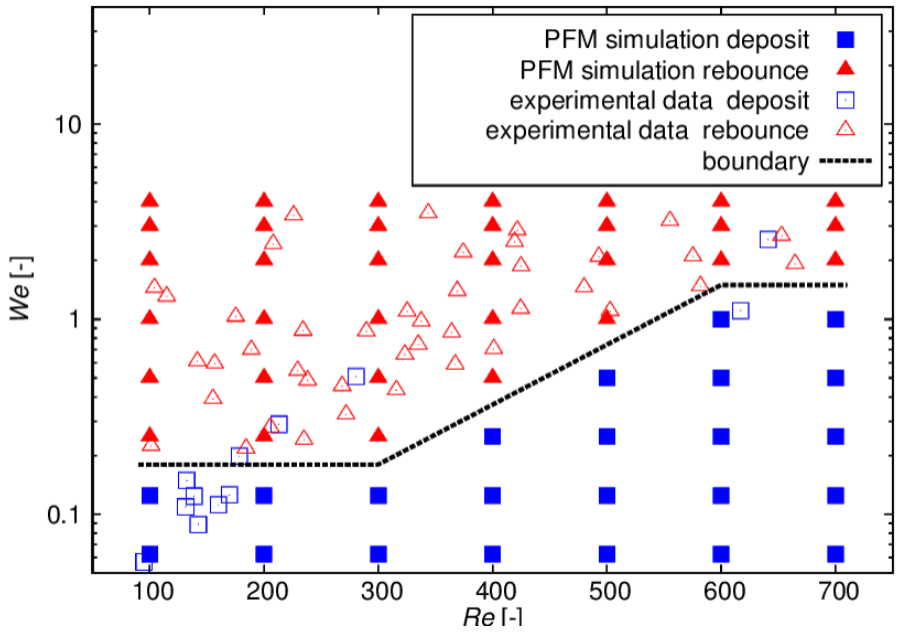


Figure 3.20.: $Re - We$ regime map. $\theta = 150^{o}$.

Caviezel et al. [11] have proposed a theoretical model based on energy-balance analysis to define the transition between rebounce and deposit zones depending on $We$ and contact angle $\theta$. This model describes the impact process as an interplay of kinetic and surface energies. If the initial kinetic energy is smaller than the energy gained by adhering to the wall, the droplet then deposits due to the surface tension effects. This model is only valid for low $We$, when surface tension effects dominate inertia. Gravity effects and viscous dissipation are neglected. This model can be described as follows:

$$We_{\text{deposit}} \leq \frac{3\Delta A(\theta, R)}{\pi R^2} \tag{3.3}$$

where $\Delta A(\theta, R)$ is the energy difference of the two equilibrium states, which is a function of contact angle $\theta$ and drop radius $R$ (see Appendix B). This expression corresponds to the curves in Figure 3.21 (a) and (b). In the two figures, a series of simulations are carried

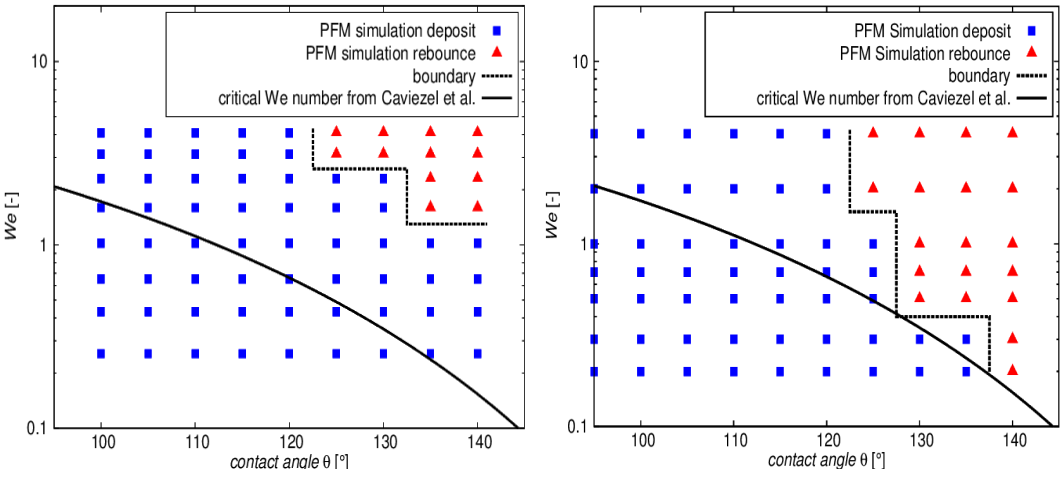


(a) $D$= 68.3 $\mu$m. (b) $D$= 2 mm.

Figure 3.21.: $We - \theta$ regime map.

out in micrometer (68.3 $\mu$m) and millimeter (2 mm) scale, respectively.

In Figure 3.21 (b), one can observe that the model of Caviezel et al. [11] and the simulation results reach good agreement when $\theta \geq 130^{o}$. Increasing the contact angle leads to a reduction of the minimum $We$ needed for rebound occurrence. In Figure 3.21 (a), where $D$= 68.3 $\mu$m, although similar conclusion can be obtained, the model of Caviezel et al. [11] underpredicts the limit line of the two zones. The micrometer-scale droplet tends to be more difficult to rebound than the millimeter-scale droplet. This finding can be explained as follows: According to Mao et al. [25], the initial impact energy of the droplet is dissipated in overcoming viscous flow and in producing new surface area. For a smaller droplet, the viscous effect takes a more important role than for larger one, more kinetic energy is therefore dissipated and then the droplet tends to deposit. With the idea of Mao et al. [25] one can also explains why the droplet in both scales tends to deposit for smaller contact angle. For small contact angle, the maximum spread factor is large, i.e., the droplet spreads over a larger area and the dissipation of energy is bigger. By comparing this two figures, it is concluded that, the model of Caviezel et al. [11] is suitable for millimeter-scale droplets. For micrometer-scale droplets, the theory is not sufficient to capture the transition from deposit to rebounce and more details must be considered to describe the droplet behavior. In this work, only the situations for low $We$ are studied. A model for higher $We$ was proposed by Mao et al. [25], who calculated energies and viscous dissipation based on empirical correlation. Comparing with the model of Mao needs much more work and time and this is not further considered in this work.

# 4. Study of Coalescence of Two Droplets

In the spray-wall-interaction of exhaust gas pipe, it is common to find coalescence of droplets (see Figure 1.1). Therefore, the coalescence of droplets is studied in this chapter. Firstly, the numerical method is validated against experimental results of Castrejón-Pita et al. [9] who studied the dynamics of the impact and coalescence of a falling droplet and a sessile droplet. Then, another validation for droplets coalescence and rebound on a superhydrophobic surface is carried out against the experiment of Peng et al. [30].

## 4.1. Validation 1: Coalescence of a Falling Droplet and a Sessile Droplet

In the experiment of Castrejón-Pita et al. [9], droplets with initial diameter of 2.38 mm were used. The droplets were made of a Newtonian mixture (water and glycerol). The distance between the respective mass centers of the two droplets (also called sideways separation or offset of droplets) between the sessile and the impacting droplet varied from 0 to 3.8 mm. Droplets were jetted on a flat polymethyl methacrylate (Perspex, Lucite) sheet. The experimental data used in the numerical validation is summarized in Table 4.1.

Table 4.1.: Experimental data used in the validation.

| Items | Values |
|---|---|
| Liquid density $\rho_l$ [kg/m$^3$] | 1222.0 |
| Liquid viscosity $\mu_l$ [mPas] | 100.0 |
| Gas density $\rho_g$ [kg/m$^3$] | 1.188 |
| Gas viscosity $\mu_g$ [mPas] | 0.0182 |
| Surface tension $\sigma$ [mN/m] | 64.0 |
| Contact angle $\theta$ [ $^o$] | 63.2 |
| Impact velocity $U$ [m/s] | 1.1 |
| Droplet diameter $D$ [mm] | 2.38 |
| Distance of droplet centers $L$ [mm] | 0.0, 0.9, 2.0, 3.0 |

Reproducing the coalescence of two droplets requires 3D simulations. Here, a half of the problem is considered with a symmetry plane (see Figure 4.1 (a)). The computational

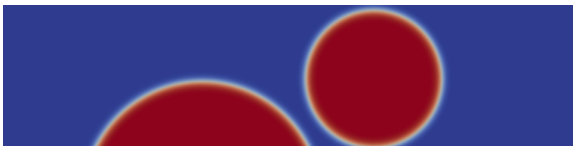

(a) Computional domain in 2D-sight.

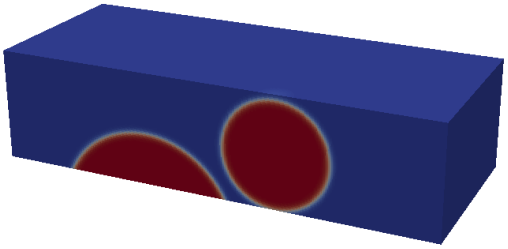

(b) Computional domain in 3D-sight.

Figure 4.1.: Computational domain (distance of droplet centers is 3 mm).

domain is a cuboid with cross section 4 mm × 10 mm and height 2.5 mm (see Figure 4.1 (b)). The whole computational domain is discretized by stationary, structured and uniform grid and the mesh spacing $h$ is $4.76 \cdot 10^{-5}$ m. Numerical parameters are set as: $Nc = 4$, $Cn = 0.02$, $\kappa = 2.266 \cdot 10^{-9}$ m$^3$s/kg. The left droplet adhering on the surface is at equilibrium. The right droplet is positioned above the surface and the height of its center is the same as the radius. The right droplet is initialized with an impact velocity of 1.1 m/s, while the velocity in the rest of the computational domain is initially zero. The boundary conditions are the same as the single droplet simulations (see chapter 3).

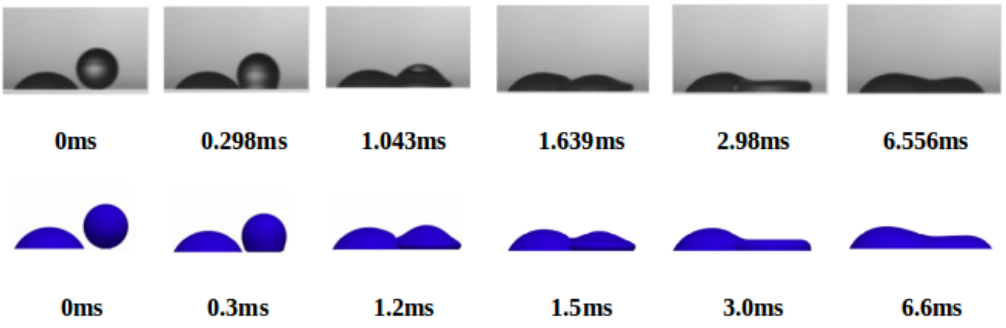


(a) Side view.

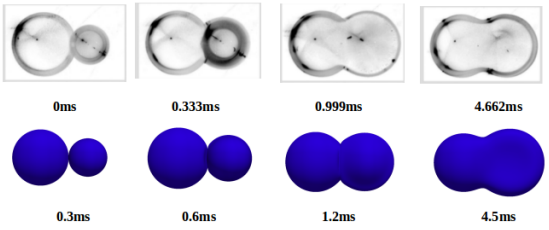


(b) Bottom view.

Figure 4.2.: Time evolution of coalescence of a falling droplet and a sessile droplet (distance of droplet centers is 3 mm). $D = 2.38$ mm, $\theta = 63.2^{\circ}$. The first rows of (a) and (b) illustrate the experimental results [9]. The droplets indicated with blue color in the second rows of (a) and (b) are the present simulation results.

Figure 4.2 shows the comparison between the present simulation and the experimental result of Castrejón-Pita et al. [9] with droplet offset of 3 mm. Figure 4.2 (a) and (b) present the side and bottom view, respectively. A good agreement is achieved. From 0 to 0.3 ms, the right droplet impacts on the surface and spreads towards the left one. Then, the two droplets begin to coalesce. The height of the impacting droplet decreases, forming a flattened disk shape, which corresponds to the maximum spreading (at the time of $t = 3$ ms). Then the height of the impacting droplet increases. After a long time of oscillation, the merger droplet reaches an equilibrium state. From the bottom view, the time evolution of the neck can be observed. The droplet edges make contact at first and then quickly form a thin bridge, this thin bridge increases in width over time until the two droplets totally merge together. During the whole process of the neck evolution, capillary, viscous and inertial forces take an important role. The impacting makes the coalescence process much quicker since the impacting droplet spreads quickly into the sessile droplet, while for the coalescence of two initially static droplets, the capillary-driven process is much slower.

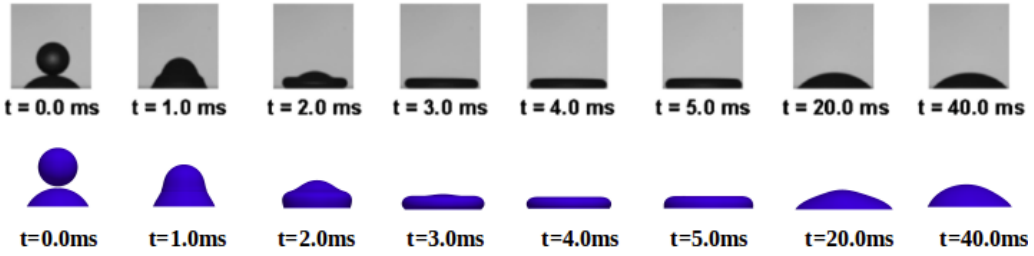


(a) Droplet separation 0 mm.

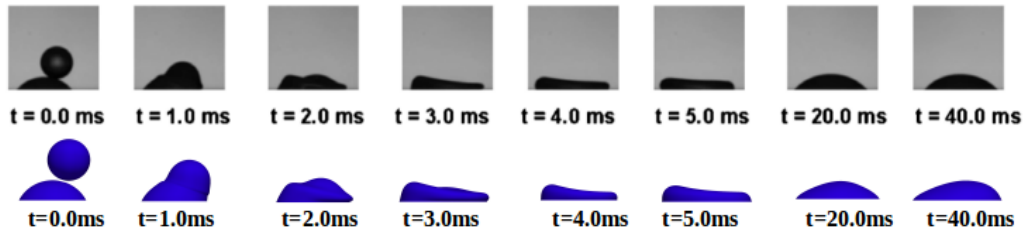


(b) Droplet separation 0.9 mm.

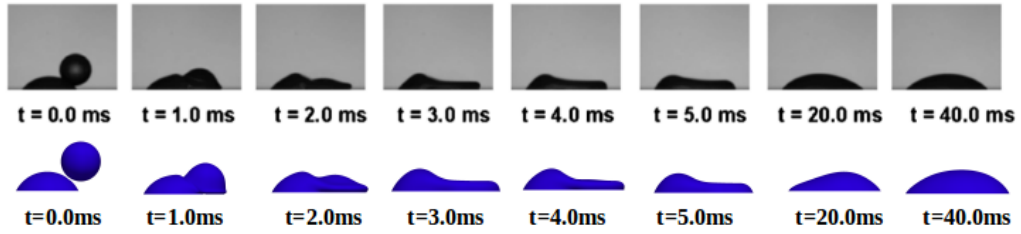


(c) Droplet separation 2 mm.

Figure 4.3.: Time evolution of coalescence of a falling droplet and a sessile droplet with different separation of droplet centers. $D = 2.38$ mm, $\theta = 63.2^{o}$. The black droplets indicate the experimental observations [9] and the blue ones present the simulation results.

Figure 4.3 illustrates the time evolution of a falling droplet and a sessile droplet with different droplet offsets and compares the present simulation results with the experimental results [9]. A very good agreement is obtained for $t \leq 5$ ms. Figure 4.3 (a) shows the situation of no offset between the centers of two droplets. The impact and coalescence process is axisymmetric. The impacting droplet lands on a surface prewetted with an equilibrium droplet and then coalesces with it. As the droplet offset is set as 0.9 mm (see

Figure 4.3 (b)), the evolution process is no longer axisymmetric. For the offset of 2 mm (see Figure 4.3 (c)), the droplets spreading and coalescence occurs at the same time. All of the coalescence processes reported here experience a long time of oscillation before a stable state is achieved ($t = 40$ ms in Figure 4.3 (a) (b) (c)). The oscillation time is longer in the simulations than in the experiment, since the surface in the simulation is set as ideally smooth and homogeneous. The roughness and heterogeneity of the surface in the experiment lead to a shorter oscillation time. From these figures, it can be concluded that the phase-field method is able to handle the coalescence problem, which involves large topological changes in free-surface shape.

## 4.2. Validation 2: Coalescence with Rebound

Peng et al. [30] conducted the droplet jumping experiment by using droplets with various volumes (from 0.2 to 10 $\mu$l). The contact angle is 158$^o$. The dynamic processes of the coalesced droplet were observed by a high speed camera system.

In the present simulations, water droplets with diameters of 1.240 mm, 1.789 mm and 2.255 mm (corresponding to 1.0, 3.0 and 6.0 $\mu$l in volume) are used. Considering the non-symmetric characteristics of the coalescence process, 3-dimensional simulations are needed. Similar to the validation in Section 4.1, the computational domain is a cuboid with cross section $3D \times D$ and height $3D$ (see Figure 4.4, $D$ is droplet diameter), which is discretized by stationary, structured and uniform grid. The mesh spacing $h$ is $2.48 \cdot 10^{-5}$ m, $3.58 \cdot 10^{-5}$ m, $4.51 \cdot 10^{-5}$ m for droplets with diameters of 1.240 mm, 1.789 mm and 2.255 mm, respectively. Numerical parameters are set as: $Nc = 4$, $Cn = 0.02$, $\kappa = 6.15 \cdot 10^{-10}$, $12.8 \cdot 10^{-10}$, $20.34 \cdot 10^{-10}$ m$^3$s/kg (for droplets with diameters of 1.240 mm, 1.789 mm and 2.255 mm, respectively.). The boundary conditions are the same as the single droplet simulations in chapter 3. The two droplets are positioned above the surface with the height of $D/2$ and the distance between the centers of the two droplets is $D$.

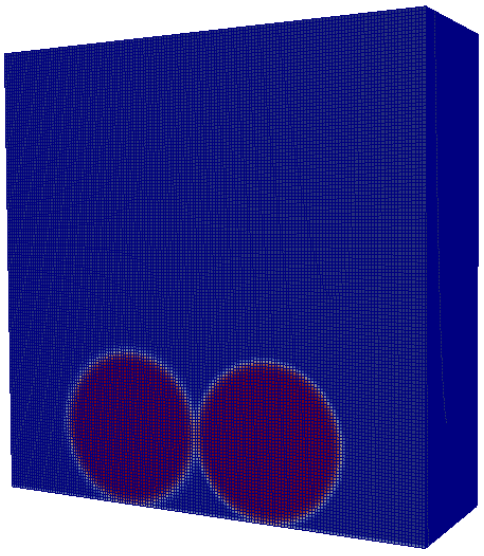

Figure 4.4.: Computational domain and the initial positions of the two droplets.

Simulations are compared with the experimental data. Figure 4.5 demonstrates the temporal evolution of the coalescence and the droplet jumping for two different diameters. The simulations agree well with the experimental observations. At the first phase of the process (Figure 4.5 (a) 0-7 ms (b) 0-10 ms), the two droplets touch each other and form a neck. As the height of the neck grows, the excess surface energy is converted into kinetic energy, leading to the jump of the coalesced droplet (Figure 4.5 (a) at the time of $t = 7$

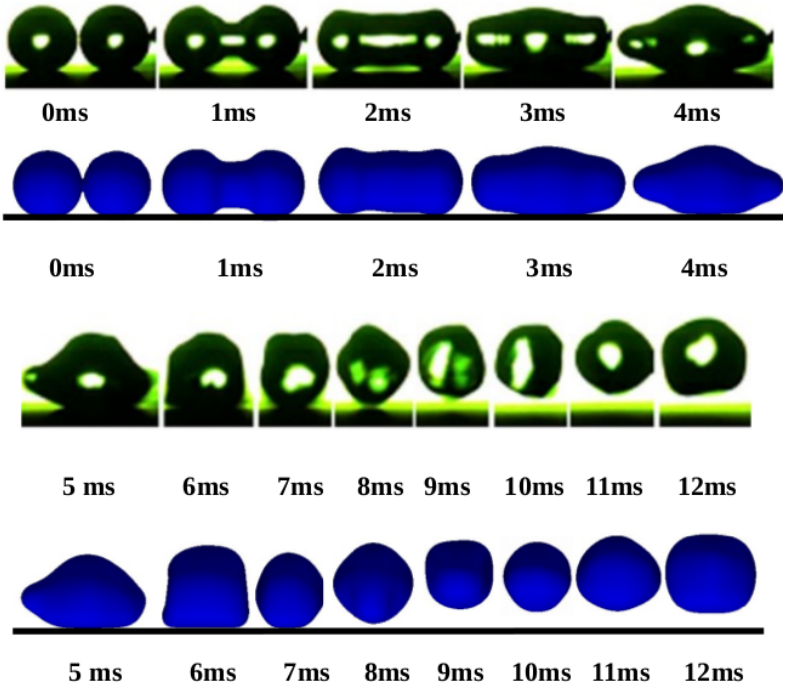


(a) $D = 1.789$ mm.

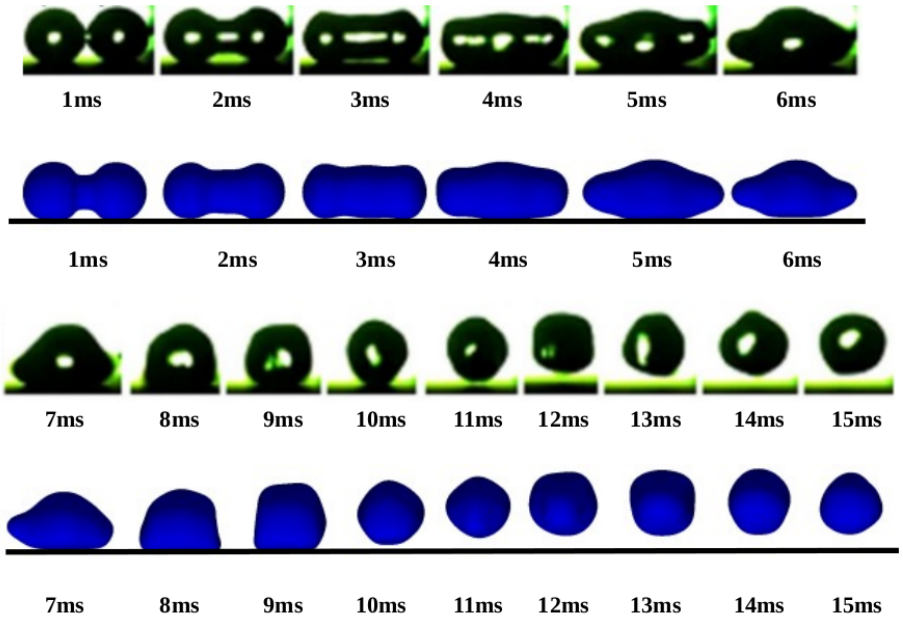


(b) $D = 2.255$ mm.

Figure 4.5.: Time evolution of coalescence and the droplet jumping. (a) droplets with diameter of 1.789 mm. (b) droplets with diameter of 2.255 mm. Initial velocity $U_0 = 0$, contact angle $\theta = 158^{\circ}$. The black droplets illustrate the experimental results [30], while the blue ones present the simulation results.

ms, Figure 4.5 (b) at the time of $t = 10$ ms). During the neck growing phase, the viscous and inertial forces take an important role. Initially, the viscous force control the neck flow dynamics. However, when the neck radius exceeds a critical value, inertia begins to dominate the flow dynamics [13]. The smaller droplet ($D = 1.789$ mm) jumps earlier than the larger one ($D = 2.255$ mm). In the following phases, the coalesced droplet jumps into the air and then falls down, after several oscillations, the droplet stays at rest. Since this process was not reported in the experiment, it is also not presented in the simulation results. From the result one can find that asymmetry shape of droplet is formed both in the experiment and the present simulations (Figure 4.5 (a) $t \geq 5$ ms (b) $t \geq 7$ ms), in spite that the initial state is symmetry. This suggest that the coalescence process may be physically not symmetric. Set sensitive to disturbances triggering the asymmetry. The phenomenon is probably due to the propagation of the capillary wave, which is generated in the coalescence process [13].

Figure 4.6 plots the dimensionless heights of the merger droplet centroid $H/D$ over time $t$ for droplets with different diameters. One can observe that the dimensionless maximum jumping height is greater for smaller droplets, which is in accordance with the conclusion of Peng et al. [30].

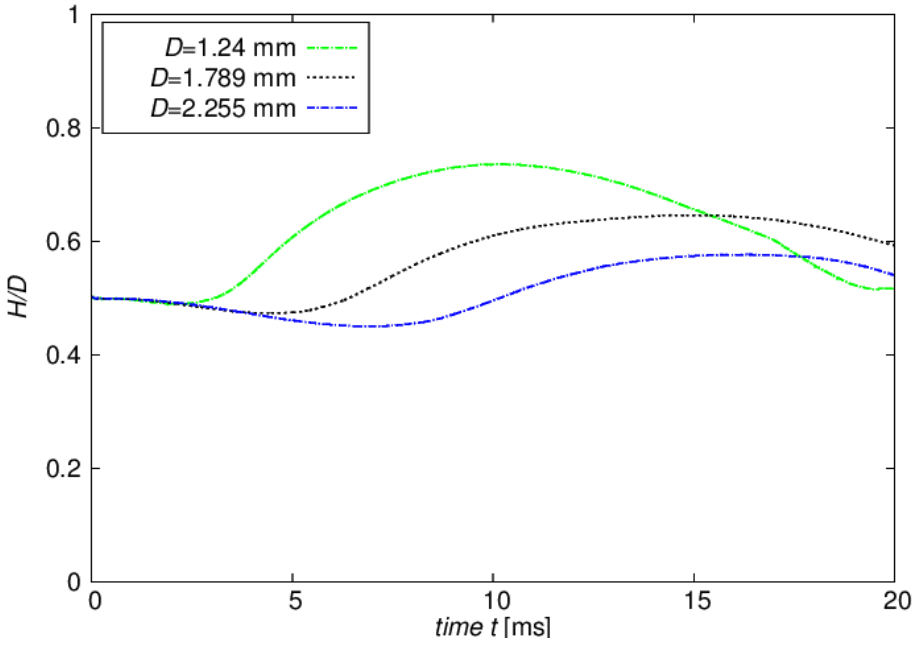


Figure 4.6.: Time evolution of dimensionless heights of the merger droplet centroid for different diameters. Initial velocity $U_0 = 0$, contact angle $\theta = 158^{\circ}$.

## 4.3. Effect of Coalescence on Rebound

In Section 4.2, numerical validation concerning coalescence with rebound is performed. However, the underlying mechanism for the coalesced droplet rebound or jumping is not discussed in detail. To further investigate the influence of the coalescence on the droplet jumping, two simulations are performed. For one, the two droplets are close enough so that coalescence occurs. For the other, they are far away from each other, so no coalescence exists. The boundary and initial conditions are the same as the cases in Section 4.2.

Figure 4.7 demonstrates the results of the two simulations. The first raw indicates the process of droplets with coalescence and the second raw shows the situation without coalescence. The time evolution of the dimensionless height of the centroid $H/D$ for droplets is illustrated in Figure 4.8. For the condition of no coalescence (red line in the

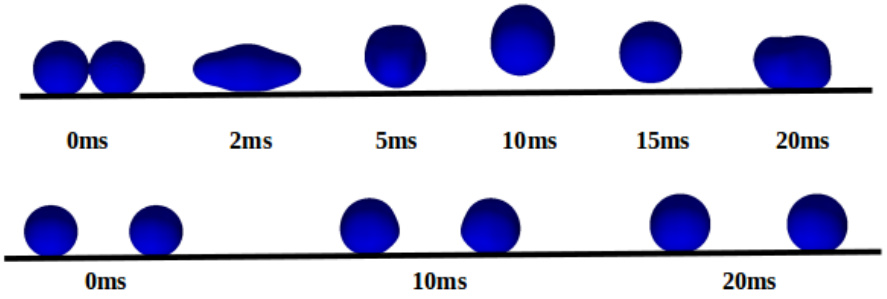


Figure 4.7.: Time evolution of two droplets with/without coalescence. Droplet diameter $D = 1.24$ mm, initial velocity $U_0 = 0$, contact angle $\theta = 158^{\circ}$.

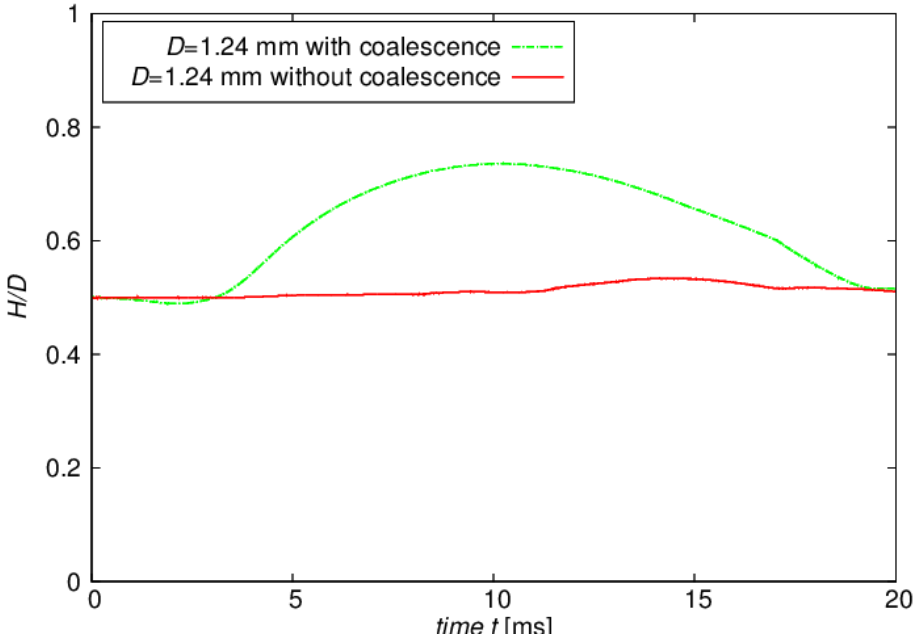


Figure 4.8.: The time evolution of the dimensionless height of the centroid for droplets in two conditions. Initial velocity $U_0 = 0$, contact angle $\theta = 158^{\circ}$.

figure), the height of centroid increases only slightly around the time $t = 15$ ms. Both of the droplets cannot jump. While for the condition of coalescence (green line in the figure), the centroid height increases rapidly to $0.75D$ and then decreases, which corresponds to the jumping and falling down of the droplet. The difference of the two lines is due to the additional energy released by the droplet coalescence. This proves that, under the present conditions, the droplet jumping is mainly driven by the coalescence process. This phenomenon is called coalescence induced droplet jumping in the literature [30].

The finding in Section 4.2 that the dimensionless maximum jumping height is greater for smaller droplets, can be therefore explained. For smaller droplets, the ratio of surface area to volume $A/V$ is greater, so that a larger fraction of the excess surface energy caused by coalescence can be converted into the effective kinetic energy, which leads to droplet jumping.

With the impact velocity varied, four groups of simulations are conducted and the results are reported in Figure 4.9. Each group consists of two simulations (with/without coalescence) under the same impact velocity. Four velocities are selected: 1, 3, 5 and 7 m/s. The dashdotted and solid curves indicate the simulations with and without coalescence, respectively. The curves with the same color belong to the same group and correspond to

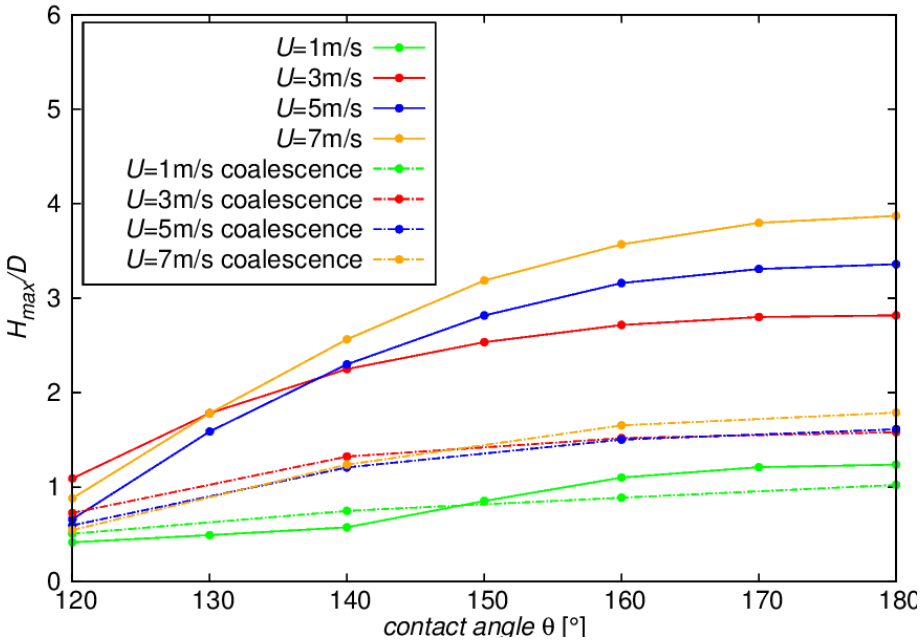


Figure 4.9.: Dimensionless maximum height of the centroid for droplets in different conditions. Droplet diameter $D = 0.0683$ mm.

the same impact velocity. One can find that the maximum centroid height of the coalesced droplet is higher than that of the droplet without coalescence when both impact velocity and contact angle are low (in Figure 4.9, $U = 1$ m/s and $120^o < \theta < 150^o$). When the impact velocity or the contact angle is higher, the existence of coalescence leads to lower maximum jumping height. This is due to the viscous dissipation of the flow during the coalescence process and the larger air friction of the coalesced droplet during the jumping process. Low impact velocity and contact angle cause less internal flow and lower jumping velocity, which yields less dissipation and lower air friction, and the energy released by coalescence is large enough left to be converted into the effective kinetic energy.

# 5. Summary and Outlook

This thesis presents numerical studies on the impact and rebound of a single droplet and coalescence of two droplets on a horizontal surface. These phenomena are very common in the spray-wall-interaction within exhaust gas pipe of SCR system. The main purpose of this study is to validate the phase-field method and gain knowledge about the underlying physics governing the rebound process and to determine under what conditions droplets can rebound.

The numerical method phase-field method is validated through three cases from literature for the single droplet impact problem. The spread factor and morphology evolution, maximal spread factor and the contact time are considered. In the first case, through the study of numerical parameters, it is found that parameters with $Nc = 6$, $Cn = 0.02$, $\kappa = 5 \cdot 10^{-10}$ m$^3$s/kg, which indicate mesh resolution, dimensionless interface width and mobility, respectively, achieve an optimal compromise between the accuracy and compute costs. The simulation results are consistent with the experimental data from literature. The second case is concerned with a correlation of maximal spread factor with $Re$ and $Oh$. The results of the present simulation under the contact angle of 35$^\circ$ agree very well with the proposed correlation, while the results of the simulations under other two larger contact angles are underpredicted the correlation especially for low $Re$ and $Oh$. This is due to the fact that the influence of wettability on the maximal spread factor becomes important when the contact line moves slowly. The third case is about contact time $T_c$ (i.e. time between impact and rebound instants). The experimental finding that the contact time of a rebounding droplet in the studied range does not depend on the impact velocity but is mainly determined by droplet radius is validated through the present simulations. The agreement is satisfactory.

After the validations, the impact behavior of a single AdBlue droplet is investigated. The impact behavior is mainly quantified through the spread factor $\beta$ and the dimensionless maximum rebound height $H_{\max}/D$ of droplets. The present study demonstrates firstly the respective effect of three physical parameters (contact angle $\theta$, impact velocity $U$ and droplet diameter $D$). With the increasing contact angle, the maximum spread factor of droplets decreases and the droplets tend to rebound easily. Increasing the impact velocity leads to faster spreading of droplets and facilitates rebounce of droplets, since sufficient kinetic energy is provided. Droplets with larger diameter have higher value of maximum spread factor and the time scale of the impact process is also larger. Furthermore, the influence of contact angle and impact velocity on the maximum rebound height of droplets is also investigated. Under the same impact velocity, the maximum rebound height increases as the contact angle is greater. In the superhydrophobic ($\theta > 140^\circ$) region, high

impact velocity leads to greater maximum rebound height. As $120^o < \theta < 140^o$, there is no monotonous relation between the maximum rebound height and the impact velocity due to the increased capillary effect.

To investigate the combined effects of the three physical parameters, a large number of simulations are performed by systematically changing the three parameters. Three regime maps for the parameters are generated, in which the deposit and rebounce zone are indicated. The boundary between the two zones demonstrates the threshold values for the transition from deposit to rebounce. The $\theta - U$ regime map reveals that droplets deposit under low contact angles ($\theta < 110^o$) and rebound under high contact angles ($\theta > 150^o$). In the region $110^o < \theta < 150^o$, the minimum impact velocity, with which the droplet can rebound, is becoming smaller as the contact angle increases. The $D - U$ regime map implies that droplets with larger diameter and impact velocity are easier to rebound. In $\theta - D$ regime map, non-monotonous relation is found between the diameter of droplets and the rebound behavior in the region of $105^o < \theta < 120^o$.

In order to clarify the underlying mechanism for the transition between the deposit and rebounce, regime maps for dimensionless parameters are generated. Through the comparison with the experiment data and theoretical model from literature [11, 35], it can be concluded that, in the studied range, the transition between the deposit and rebounce depends mainly on Weber number $We$, contact angle $\theta$ and the droplet size scale.

The numerical method is applied for droplets coalescence problems. These include coalescence of a falling droplet and a sessile one with different droplet center distances and coalescence with rebound for different droplet diameters. The present numerical results and the experimental data from literature show a very good agreement. Afterwards, the effect of coalescence on the rebound behavior of droplets is investigated. The coalescence process can release energy due to the excessive surface energy. At the same time, it can also bring about viscous dissipation and additional air friction. Coalescence of droplets without or with very low impact velocity can therefore promote the rebound.

In this work, the PFM has shown its great advantages in handling the droplet impact, rebound and coalescence problems. The present investigations in this thesis are reliable and can provide useful information to the related research.

The simulations for a single Adblue droplet in this thesis are performed in the range of 0.01 m/s $\leq U \leq$ 10 m/s, 0.01 mm$\leq D \leq$3 mm, which covers the variation range of droplet diameter and impact velocity in SCR system. However, all the simulations in this study are carried out on ideally smooth surfaces. In further works, surfaces with micro-structure can be considered. Besides, the droplets in this study impact normal to the surface. The effect of different impact angles can be studied in future. Furthermore, the present simulations only concern about the isothermal process. The heat transfer phenomena takes an important role in the spray-wall-interaction in most situations in industrial applications. Taking account of the hydrodynamics coupled with heat transfer is of great significance for accurately describing the spray-wall-interaction.

# Symbols and Abbreviations

## Latin Symbols

| | | |
|---|---|---|
| $A$ | [$m^2$] | surface area |
| $C$ | [-] | order parameter |
| $Ca$ | [-] | Capillary number |
| $Cn$ | [-] | Cahn number |
| $D$ | [mm] | droplet diameter |
| $D_0$ | [mm] | initial droplet diameter |
| $D_t$ | [mm] | instantaneous base diameter |
| $E_0$ | [J] | total equilibrium energy of a free drop |
| $E_1$ | [J] | total equilibrium energy of a drop adhering to a wall |
| $E_k$ | [J] | initial kinetic energy |
| $\Delta E$ | [J] | energy difference between two equilibrium states |
| $f$ | [$J/m^3$] | free energy density |
| $\vec{f_\sigma}$ | [$N/m^3$] | interfacial force |
| $F$ | [J] | free energy |
| $Fr$ | [-] | Froude number |
| $\vec{g}$ | [$m/s^2$] | gravitational acceleration |
| $h$ | [m] | mesh spacing |
| $H$ | [m] | droplet jumping height |
| $H_{\max}$ | [m] | droplet maximum jumping height |
| $L$ | [m] | reference length |
| $L_c$ | [m] | interface width |
| $\vec{n_s}$ | [-] | normal vector of the wall |
| $Nc$ | [-] | number of mesh cells per interface width |
| $N_d$ | [-] | number of mesh cells per droplet diameter |
| $Oh$ | [-] | Ohnesorge number |
| $p$ | [Pa] | pressure |
| $R$ | [mm] | droplet radius |
| $Re$ | [-] | Reynolds number |
| $St$ | [-] | Stokes number |
| $t$ | [ms] | time |
| $t^*$ | [-] | dimensionless time |
| $T_c$ | [ms] | contact time |
| $\vec{u}$ | [m/s] | velocity field |
| $U$ | [m/s] | impact velocity |
| $V$ | [$m^3$] | volume |
| $We$ | [-] | Weber number |
| $x$ | [m] | x-coordinate |

## Greek Symbols

| | | |
|---|---|---|
| $\beta$ | [-] | spread factor |

| | | |
|---|---|---|
| $\beta_{\max}$ | [-] | maximal spread factor |
| $\gamma_{SV}$ | [mN/m] | solid-gas interfacial tension |
| $\gamma_{LV}$ | [mN/m] | liquid-gas interfacial tension |
| $\gamma_{SL}$ | [mN/m] | liquid-solid interfacial tension |
| $\varepsilon$ | [m] | capillary width |
| $\theta$ | [°] | contact angle |
| $\theta_A$ | [°] | advancing contact angle |
| $\theta_R$ | [°] | receding contact angle |
| $\kappa$ | [$m^3$s/kg] | mobility |
| $\lambda$ | [J/m] | mixing energy parameter |
| $\mu$ | [Pas] | dynamical viscosity |
| $\nu$ | [$m^2$/s] | kinematic viscosity |
| $\pi$ | [-] | the circular ratio |
| $\rho$ | [kg/$m^3$] | density |
| $\sigma$ | [mN/m] | surface tension |
| $\phi$ | [J/$m^3$] | Cahn-Hilliard chemical potential |

## Subscripts

| | |
|---|---|
| g | gas phase |
| l | liquid phase |
| max | maximal |

## Abbreviations

| | |
|---|---|
| 2D | Two Dimensional |
| 3D | Three Dimensional |
| CFD | Computational Fluid Dynamics |
| CH | Cahn-Hilliard equation |
| $NO_x$ | Nitrogen Oxides |
| NS | Navier-Stokes equations |
| OpenFOAM | Open Source Field Operation And Manipulation |
| PFM | Phase-Field Method |
| SCR | Selective Catalytic Reduction |
| VOF | Volume-of-Fluid Method |

# List of Figures


1.1. Spray/Wall-Interaction. Taken from [47]. . . . . 1

2.1. Lotus effect. Taken from [5]. . . . . 3
2.2. A drop on a flat surface. Taken from [23]. . . . . 4
2.3. Contact angle and wettability. Taken from [23]. . . . . 4
2.4. Morphology of droplet impact on a dry surface. Taken from [34]. . . . . 6
2.5. Time evolution of spread factor. Taken from [33]. . . . . 7
2.6. Instant states of droplet of the present simulation. (a) The initial state. (b) The kinematic phase. (c) The spreading phase. (d) The maximum spreading. (e) The relaxation phase. (f) The wetting/equilibrium phase. . 7
2.7. Bird-View onto the coalescence of two drops on a horizontal surface. Taken from [10]. . . . . 8
2.8. Diffuse and sharp interface model. Taken from [29]. . . . . 8
2.9. Distribution of $C$ for a droplet. . . . . 9

3.1. Computational domain and boundary conditions. . . . . 13
3.2. Influence of mesh resolution on time evolution of spread factor. $Cn = 0.02$ and $\kappa = 2.8 \cdot 10^{-9}$ m$^3$s/kg. . . . . 14
3.3. Influence of Cahn number on time evolution of spread factor. $Nc = 6$ and $\kappa = 2.8 \cdot 10^{-9}$ m$^3$s/kg. . . . . 14
3.4. Influence of mobility factor on time evolution of spread factor. $Cn = 0.02$ and $N_c = 6$. . . . . 15
3.5. Time evolution of the droplet shape from side view. The first and third rows with black droplets indicate the experimental result [46]. The second and last rows with blue ones illustrate the present numerical result. . . . . 15
3.6. Drop volume conservation in the simulation. $V_0$ is initial drop volume and $V$ is instantaneous drop volume. . . . . 16
3.7. Maximal spread factor correlated against $Re^2Oh$. . . . . 17
3.8. Time evolution of the droplet shape. The first and fourth picture indicate the impact and rebound instant, respectively. $T_c$ is contact time. . . . . 17
3.9. Influence of contact angle on the contact time. Droplet diameter $D = 0.2$ mm, impact velocity $U = 2$ m/s. . . . . 18
3.10. Contact time of bouncing drops with different radii. The different lines indicate the average contact time. Contact angle $\theta = 170^o$. . . . . 19
3.11. Contact time of a bouncing drop as a function of drop radius. Contact angle of the present simulation $\theta = 170^o$. . . . . 19
3.12. Influence of contact angle on droplet behavior. $D = 0.0683$ mm, $U = 7.228$ m/s. $T_c$ is contact time. (see Figure 3.8.) . . . . . 20
3.13. Influence of impact velocity on droplet behavior. $D = 0.0683$ mm, $\theta = 130^o$. $T_c$ is contact time. . . . . 21
3.14. Influence of diameter on droplet behavior. $\theta = 130^o$, $U = 5$ m/s. . . . . 22
3.15. Air film beneath the droplet with diameter of 0.8 mm around $t = 1.6$ ms. . 22

3.16. Influence of contact angles and impact velocities on dimensionless maximum rebound height. Droplet diameter $D = 0.0683$ mm. . . . . 23
3.17. $\theta - U$ regime map. $D = 0.0683$ mm. . . . . 23
3.18. $D - U$ regime map. $\theta = 130^o$. . . . . 24
3.19. $\theta - D$ regime map. $U = 7.228$ m/s. . . . . 25
3.20. $Re - We$ regime map. $\theta = 150^o$. . . . . 26
3.21. $We - \theta$ regime map. . . . . 26

4.1. Computational domain (distance of droplet centers is 3 mm). . . . . 29
4.2. Time evolution of coalescence of a falling droplet and a sessile droplet (distance of droplet centers is 3 mm). $D = 2.38$ mm, $\theta = 63.2^o$. The first rows of (a) and (b) illustrate the experimental results [9]. The droplets indicated with blue color in the second rows of (a) and (b) are the present simulation results. . . . . 29
4.3. Time evolution of coalescence of a falling droplet and a sessile droplet with different separation of droplet centers. $D = 2.38$ mm, $\theta = 63.2^o$. The black droplets indicate the experimental observations [9] and the blue ones present the simulation results. . . . . 30
4.4. Computational domain and the initial positions of the two droplets. . . . . 31
4.5. Time evolution of coalescence and the droplet jumping. (a) droplets with diameter of 1.789 mm. (b) droplets with diameter of 2.255 mm. Initial velocity $U_0 = 0$, contact angle $\theta = 158^o$. The black droplets illustrate the experimental results [30], while the blue ones present the simulation results. 32
4.6. Time evolution of dimensionless heights of the merger droplet centroid for different diameters. Initial velocity $U_0 = 0$, contact angle $\theta = 158^o$. . . . . 33
4.7. Time evolution of two droplets with/without coalescence. Droplet diameter $D = 1.24$ mm, initial velocity $U_0 = 0$, contact angle $\theta = 158^o$. . . . . 34
4.8. The time evolution of the dimensionless height of the centroid for droplets in two conditions. Initial velocity $U_0 = 0$, contact angle $\theta = 158^o$. . . . . 34
4.9. Dimensionless maximum height of the centroid for droplets in different conditions. Droplet diameter $D = 0.0683$ mm. . . . . 35

B.1. Equilibrium shapes of a liquid drop surrounded by gas and a drop adhered to a wall, neglecting gravitational effects. Taken from [11]. . . . . 47

# List of Tables

3.1. Physical properties of the fluids. . . . . 12
3.2. Parameters for AdBlue droplet simulations. . . . . 20

4.1. Experimental data used in the validation. . . . . 28

# Bibliography


[1] C. Antonini, A. Amirfazli, and M. Marengo. Drop impact and wettability: From hydrophilic to superhydrophobic surfaces. *Physics of Fluids*, 24(10):102104, 2012.

[2] R. Bernard. Phasenfeld simulation eines tropfenaufpralls auf strukturierten oberflächen. Masterarbeit, Karlsruher Institute für Technologie, 2016.

[3] F. Birkhold, U. Meingast, P. Wassermann, and O. Deutschmann. Analysis of the injection of urea-water-solution for automotive SCR DeNOx-systems: modeling of two-phase flow and spray/wall-interaction. Technical report, SAE Technical Paper, 2006.

[4] F. Birkhold, U. Meingast, P. Wassermann, and O. Deutschmann. Modeling and simulation of the injection of urea-water-solution for automotive SCR DeNOx-systems. *Applied Catalysis B: Environmental*, 70(1):119–127, 2007.

[5] D. Bonn, J. Eggers, J. Indekeu, J. Meunier, and E. Rolley. Wetting and spreading. *Reviews of Modern Physics*, 81(2):739, 2009.

[6] X. Cai, H. Marschall, M. Wörner, and O. Deutschmann. Numerical simulation of wetting phenomena with a phase-field method using OpenFOAM®. *Chemical Engineering & Technology*, 38(11):1985–1992, 2015.

[7] X. Cai, M. Wörner, H. Marschall, and O. Deutschmann. Numerical study on the wettability dependent interaction of a rising bubble with a periodic open cellular structure. *Catalysis Today*, 273:151–160, 2016.

[8] X. Cai, M. Wörner and O. Deutschmann. Implementation of a phase field method in OpenFOAM® for simulation of spreading droplets and verification by test problems. *In Proceedings of 7th Open Source CFD International Conference, Hamburg,* 2013.

[9] J.R. Castrejón-Pita, E.S. Betton, K.J. Kubiak, M.C.T. Wilson, and I.M. Hutchings. The dynamics of the impact and coalescence of droplets on a solid surface. *Biomicrofluidics*, 5(1):014112, 2011.

[10] J.R. Castrejón-Pita, K.J. Kubiak, A.A. Castrejón-Pita, M.C.T. Wilson, and I.M. Hutchings. Mixing and internal dynamics of droplets impacting and coalescing on a solid surface. *Physical Review E*, 88(2):023023, 2013.

[11] D. Caviezel, C. Narayanan, and D. Lakehal. Adherence and bouncing of liquid droplets impacting on dry surfaces. *Microfluidics and Nanofluidics*, 5(4):469–478, 2008.

[12] O. Deutschmann, J. Grunwaldt, et al. Exhaust gas aftertreatment in mobile systems: Status, challenges, and perspectives. *Chemie Ingenieur Technik*, 85(5):595–617, 2013.

[13] R. Enright, N. Miljkovic, J. Sprittles, K. Nolan, R. Mitchell, and E.N. Wang. How coalescing droplets jump. *ACS nano*, 8(10):10352–10362, 2014.

[14] D. Jacqmin. Calculation of two-phase navier–stokes flows using phase-field modeling. *Journal of Computational Physics*, 155(1):96–127, 1999.

[15] D. Jacqmin. Contact-line dynamics of a diffuse fluid interface. *Journal of Fluid Mechanics*, 402:57–88, 2000.

[16] C. Josserand and S.T. Thoroddsen. Drop impact on a solid surface. *Annual Review*

*of Fluid Mechanics*, 48:365–391, 2016.

[17] V.V. Khatavkar, P.D. Anderson, and H.E.H. Meijer. Capillary spreading of a droplet in the partially wetting regime using a diffuse-interface model. *Journal of Fluid Mechanics*, 572:367–387, 2007.

[18] K. Koch, B. Bhushan, and W. Barthlott. Diversity of structure, morphology and wetting of plant surfaces. *Soft Matter*, 4(10):1943–1963, 2008.

[19] M. Koebel, M. Elsener, and M. Kleemann. Urea-scr: a promising technique to reduce NOx emissions from automotive diesel engines. *Catalysis Today*, 59(3):335–345, 2000.

[20] M. Koebel, M. Elsener, and T. Marti. NOx-reduction in diesel exhaust gas with urea and selective catalytic reduction. *Combustion Science and Technology*, 121(1-6):85–102, 1996.

[21] H. Kusumaatmaja, E.J. Hemingway and S.M. Fielding. Moving contact line dynamics: from diffuse to sharp interfaces. *Journal of Fluid Mechanics*, 788:209–227, 2016.

[22] K. Law and H. Zhao. *Surface wetting: characterization, contact angle, and fundamentals*, Springer, 2015.

[23] H.J. Lee and S. Michielsen. Lotus effect: superhydrophobicity. *Journal of the Textile Institute*, 97(5):455–462, 2006.

[24] J. Lowengrub and L. Truskinovsky. Quasi–incompressible cahn–hilliard fluids and topological transitions. In *Proceedings of the Royal Society of London A: Mathematical, Physical and Engineering Sciences*, volume 454, pages 2617–2654. The Royal Society, 1998.

[25] T. Mao, D. Kuhn, and H. Tran. Spread and rebound of liquid droplets upon impact on flat surfaces. *AIChE Journal*, 43(9):2169–2179, 1997.

[26] M. Marengo, C. Antonini, I.V. Roisman, and C. Tropea. Drop collisions with simple and complex surfaces. *Current Opinion in Colloid & Interface Science*, 16(4):292–302, 2011.

[27] H. Marschall, X. Cai, M. Wörner, and O. Deutschmann. Conservative finite volume discretization of the two-phase navier-stokes cahn-hilliard and allen-cahn equations on general grids with applications to dynamic wetting (2016).

[28] H. Marschall, X. Cai, M. Wörner, and O. Deutschmann. Development of phase field methods using OpenFOAM® - part i: method development and implementation. in: 10th international OpenFOAM® workshop, ann arbor, michigan, usa, 2015.

[29] N. Moelans, B. Blanpain, and P. Wollants. An introduction to phase-field modeling of microstructure evolution. *Calphad*, 32(2):268–294, 2008.

[30] B. Peng, S. Wang, Z. Lan, W. Xu, R. Wen, and X. Ma. Analysis of droplet jumping phenomenon with lattice boltzmann simulation of droplet coalescence. *Applied Physics Letters*, 102(15):151601, 2013.

[31] L. Rayleigh. On the capillary phenomena of jets. In *Proc. R. Soc. London*, volume 29, pages 71–97, 1879.

[32] D. Richard, C. Clanet, and D. Quéré. Surface phenomena: Contact time of a bouncing drop. *Nature*, 417(6891):811–811, 2002.

[33] R. Rioboo, M. Marengo, and C. Tropea. Time evolution of liquid drop impact onto solid, dry surfaces. *Experiments in Fluids*, 33(1):112–124, 2002.

[34] R. Rioboo, C. Tropea, and M. Marengo. Outcomes from a drop impact on solid surfaces. *Atomization and Sprays*, 11(2), 2001.

[35] R. Rioboo, M. Voué, A. Vaillant, and J. De Coninck. Drop impact on porous superhydrophobic polymer surfaces. *Langmuir*, 24(24):14074–14077, 2008.

[36] B.L. Scheller and D.W. Bousfield. Newtonian drop impact with a solid surface. *AIChE*

*Journal*, 41(6):1357–1367, 1995.

[37] M. Sellier and E. Trelluyer. Modeling the coalescence of sessile droplets. *Biomicrofluidics*, 3(2):022412, 2009.

[38] R. Tadmor. Line energy and the relation between advancing, receding, and young contact angles. *Langmuir*, 20(18):7659–7664, 2004.

[39] W. Villanueva and G. Amberg. Some generic capillary-driven flows. *International Journal of Multiphase Flow*, 32(9):1072–1086, 2006.

[40] L.H.J. Wachters and N.A.J. Westerling. The heat transfer from a hot wall to impinging water drops in the spheroidal state. *Chemical Engineering Science*, 21(11):1047–1056, 1966.

[41] A.M. Worthington. On the forms assumed by drops of liquids falling vertically on a horizontal plate. *Proceedings of the Royal Society of London*, 25(171-178):261–272, 1876.

[42] A.L. Yarin. Drop impact dynamics: splashing, spreading, receding, bouncing.... *Annu. Rev. Fluid Mech.*, 38:159–192, 2006.

[43] T. Young. An essay on the cohesion of fluids. *Philosophical Transactions of the Royal Society of London*, 95:65–87, 1805.

[44] P. Yue and J.J. Feng. Can diffuse-interface models quantitatively describe moving contact lines? *The European Physical Journal-Special Topics*, 197(1):37–46, 2011.

[45] P. Yue, J.J. Feng, C. Liu, and J. Shen. A diffuse-interface method for simulating two-phase flows of complex fluids. *Journal of Fluid Mechanics*, 515:293–317, 2004.

[46] D. Zang, X. Wang, X. Geng, Y. Zhang, and Y. Chen. Impact dynamics of droplets with silica nanoparticles and polymer additives. *Soft Matter*, 9(2):394–400, 2013.

[47] Y. Zhang, M. Jia, H. Liu, and M. Xie. Development of an improved liquid film model for spray/wall interaction under engine-relevant conditions. *International Journal of Multiphase Flow*, 79:74–87, 2016.

# Appendix

## A. OpenFOAM Codes

The codes for capturing the base diameter and centroid height of a droplet are listed in this part.

### A.1. Function for capturing the base diameter of a droplet

```
functions
(
radius
{
type swakExpression;
// outputControl runTime;
valueType set;
verbose true;
setName surface;

set
{
type uniform;
axis x;
start (0 0 0);
end (5e-3 0 0);
// nPoints 10000;
nPoints 100000;
}
expression "(C > 0) ? (pos().x ) : 0";
accumulations (max);
interpolate true;
interpolationType cellPoint;
}
);
```

### A.2. Function for capturing the height of droplet centroid

```
functions
(
dropletCentreZ
{
type swakExpression;
valueType internalField;
verbose true;
variables (
"Vol= sum (C > 0 ? vol() : 0);"
"VolZ= sum (C > 0 ? pos().z*vol() :
0);"
);
expression "VolZ/Vol";
accumulations (
min
);
}
);
```

## B. The Regime Limit Model of Caviezel

The model of Caviezel et al. [11] is a simple estimation to determine the limit between rebounce and deposit regimes by comparing the initial kinetic energy $E_k$ of the drop to the surface energy difference $\Delta E = \Delta A \gamma_{LV}$ of a spherical drop at equilibrium, and a drop adhering to a wall, at equilibrium (see Figure B.1).

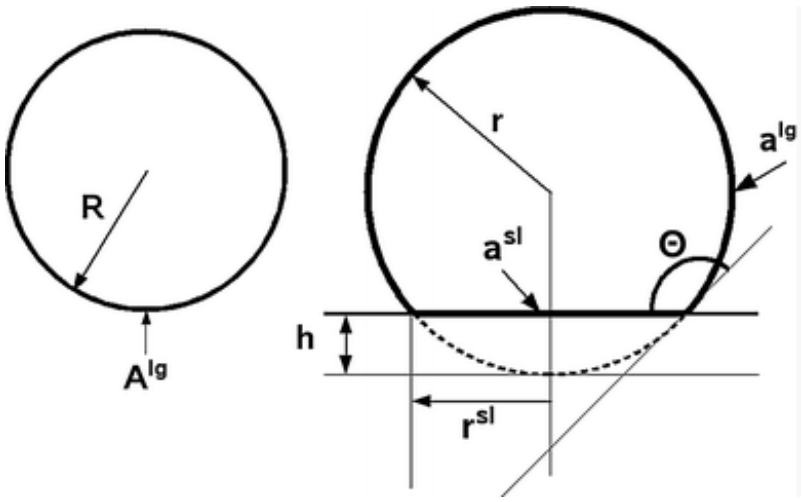


Figure B.1.: Equilibrium shapes of a liquid drop surrounded by gas and a drop adhered to a wall, neglecting gravitational effects. Taken from [11].

According to Caviezel et al. [11], the total equilibrium energy of a free drop is given by

$$E_0 = 4\pi R^2 \gamma_{LV} \tag{B.1}$$

and the equilibrium state of the drop adhering to the wall is given by

$$E_1 = (4\pi r^2 - 2\pi r h)\gamma_{LV} + \pi (r^{sl})^2 (\gamma_{SL} - \gamma_{SV}) \tag{B.2}$$

Young's equation:

$$(\gamma_{SL} - \gamma_{SV}) = -\gamma_{LV} \cos\theta \tag{B.3}$$

Droplet in the two states has the same volume, then we can obtain

$$r = 2R[2(1 - \cos\theta)(2 - \cos\theta - \cos^2\theta)]^{-1/3} \tag{B.4}$$

The surface energy difference $\Delta E = E_0 - E_1 = \Delta A \gamma_{LV}$, we obtain:

$$\Delta E = 4\pi R^2 \gamma_{LV} \{1 - (2 - 3\cos\theta + \cos^3\theta)[2(1 - \cos\theta)(2 - \cos\theta - \cos^2\theta)]^{-2/3}\} \tag{B.5}$$

Therefore:

$$\Delta A = 4\pi R^2 \{1 - (2 - 3\cos\theta + \cos^3\theta)[2(1 - \cos\theta)(2 - \cos\theta - \cos^2\theta)]^{-2/3}\} \tag{B.6}$$

$\Delta A = \Delta A(\theta, R)$ is only the function of contact angle $\theta$ and droplet radius $R$. If the initial kinetic energy $E_k \leq \Delta E$, the droplet deposits to the surface. The equation $E_k \leq \Delta E$ can also described as Equation 3.3 with a limit for $We$.